Chemical Engineering Science 338 (2027) 124647

Contents lists available at ScienceDirect

Chemical Engineering Science

journal homepage: www.elsevier.com/locate/ces

# High-resolution numerical simulations of turbulent non-catalytic reverse water-gas-shift

Nils Erland L. Haugen [a,b,*], Axel Brandenburg [c], Ewa Karchniwy [a], Ole Hauke Heinz Meyer [a], Åsmund Ervik [a], Hursanay Fyhn [a], Ladan Samaei [d], Bjørn Bringedal [d]

[a] SINTEF Energy Research, Trondheim, Norway
[b] Division of Energy Science, Luleå University of Technology, Luleå, Sweden
[c] Nordita, Stockholm, Sweden
[d] Nordic Electrofuel AS, Oslo, Norway

ARTICLE INFO

*Keywords:*
E-SAF
Reverse water-gas-shift
Hydrogen
Carbon-dioxide
DNS
LES

ABSTRACT

A green transition in aviation requires a drastic upscaling of Sustainable Aviation Fuel (SAF). The power-to-liquid process for the production of $CO_2$-neutral jet fuel via electricity, called electro-SAF (e-SAF), directly replaces fossil jet fuel without having to change infrastructure, aeroplanes, or jet-engines. The process combines green hydrogen with industrial exhaust gas, or captured carbon dioxide, in a circular economy concept. A key element of the e-SAF production plant is the reactor where syngas is produced. Traditional reactors use catalytic technology, which faces severe challenges due to the reduced performance over time because of catalyst degradation, clogging, and breakup due to embrittlement. This results in large operational costs and low process efficiency. A high-potential alternative is the catalyst-free reverse water-gas-shift (RWGS) reactor concept, which has key advantages in energy efficiency, flexibility of operation, potential for upscaling, and applications in related fields.

The primary aim of this paper is to investigate the fundamental aspects of the catalyst-free (non-catalytic) RWGS process, such as reaction kinetics and the interactions between turbulence and chemistry. The secondary aim is to identify how a typical combustion subgrid scale models for Large Eddy Simulations (LES) perform when the chemical reactions are endothermic, in contrast to the strong endothermicity associated with classical combustion. This is done by comparing results from LES with corresponding Direct Numerical Simulations (DNS), which does not rely on any turbulence modeling.

It is found that even small traces of $O_2$ in the $CO_2$ stream can significantly increase the production rate of CO. This is attributed to the increased pool of OH, which benefits the CO production rate. The effect is strongest at atmospheric pressure and less pronounced at higher pressure.

By using the temporal jet framework to study turbulence-chemistry interactions, an algebraic equation for the prediction of the CO conversion time in a turbulent flow as a function of Damköhler number and chemical timescale is employed. This allows for an *a priori* estimation of the required residence time to reach full conversion of the RWGS reaction for various turbulent shear flows.

Finally, except for some smaller systematic deviations, it is concluded that the partially stirred reactor (PaSR) LES subgrid model designed for combustion reactions perform well also for the endothermic reverse water-gas-shift reaction.

## 1. Introduction

Carbon dioxide ($CO_2$), extracted directly from the atmosphere or captured from industrial emissions, can be used as a source of carbon for the production of useful organic chemicals, such as methane and other hydrocarbons. Conversion of $CO_2$ into valuable products can be realized in different ways. One way is to convert $CO_2$ directly to methane through the Sabatier process:

$$CO_2 + 4H_2 \Leftrightarrow CH_4 + 2H_2O. \quad (1)$$

A direct synthesis of methane through $CO_2$ hydrogenation is typically characterized by a low $CO_2$ conversion and relatively low selectivity of methane, even at high pressure and elevated temperature (Fayisa et al., 2022). The requirement for a high $H_2$ concentration and operating pres-

* Corresponding author.
*E-mail address:* nils.e.haugen@sintef.no (N.E.L. Haugen).

https://doi.org/10.1016/j.ces.2026.124647
Received 4 March 2026; Received in revised form 23 June 2026; Accepted 11 July 2026
Available online 12 July 2026

**Nomenclature**

| | |
|---|---|
| $\rho$ | Fluid density |
| $\boldsymbol{u}$ | Fluid velocity |
| $P$ | Pressure |
| $\boldsymbol{F}_{\text{visc}}$ | Viscous force |
| $S$ | Traceless rate of strain tensor |
| $Y_k$ | Mass fraction of species $k$ |
| $X_k$ | Mole fraction of species $k$ |
| $\boldsymbol{J}_k$ | Diffusive flux of species $k$ |
| $\dot{\omega}_k$ | Reaction rate of species $k$ |
| $T$ | Temperature |
| $R$ | Gas constant |
| $c_p$ | Heat capacity at constant pressure |
| $m_k$ | Molar mass of species $k$ |
| $m$ | Mean molar mass of mixture |
| $h_k$ | Enthalpy of species $k$ |
| $\boldsymbol{q}$ | Heat flux |
| $\lambda$ | Thermal conductivity |
| $\kappa$ | PaSR correction factor for turbulence-chemistry interactions |
| $\tau_{\text{c}}$ | Chemical timescale |
| $\tau_{\text{mix}}$ | Timescale of turbulent mixing used in PaSR model |
| $\tau_{\text{f}}$ | Fluid timescale, based on initial jet dimension and velocity |
| $C_{\text{mix}}$ | Free parameter used to estimate $\tau_{\text{mix}}$ |
| Re | Reynolds number |
| $z_{\text{H}}$ | Mixture fraction based on hydrogen |
| $N_{\text{spec}}$ | Number of species |
| FI | Flame index |
| $[X]$ | Concentration of species X |
| $k$ | Reaction rate |
| $k_0$ | Pre-exponential factor for Arrhenius expression |
| $E$ | Activation energy |
| Da | Damkohler number |
| $V$ | Volume of grid cell |
| $V_{\text{domain}}$ | Volume of computational domain |
| $L_j$ | Length of domain in direction $j$ |
| $H_{\text{jet,u}}$ | Initial height of jet based on velocity |
| $H_{\text{jet,sc}}$ | Initial height of jet based on the scalars |
| $t_{\text{CO}}$ | Time to reach 95% yield of CO |
| $t_{\text{CO,app}}$ | Time to reach 95% yield of CO based on empirical expression |
| $\alpha$ | Empirical fitting value for expression for $t_{\text{CO,app}}$ |

sure makes the process expensive. Another approach involves converting $CO_2$ to CO by means of the reverse water-gas-shift (RWGS) reaction, thereby producing synthesis gas (syngas), a mixture of CO and hydrogen:

$$CO_2 + H_2 \Leftrightarrow CO + H_2O \tag{2}$$

and further transform the products into synthetic fuels, such as methane and other hydrocarbons, for example via methanation and Fischer–Tropsch synthesis. The RWGS reaction requires less $H_2$, and the produced CO gives a high flexibility for further transformation (Benzinger et al., 2019; Desgagnés et al., 2024). To achieve a high $CO_2$ conversion, a high temperature is required as the RWGS reaction is endothermic, and thermodynamic equilibrium shifts towards CO when the temperature increases.

The reaction is typically carried out in catalytic, fixed-bed reactors, in which various catalysts can be used to enhance the reaction rate and CO selectivity. In this context, a fixed-bed reactor means a chemical reactor that holds a stationary bed of solid particles through which gaseous reactants flow continuously. In recent studies, a selectivity of nearly 100% is demonstrated: 96.41% by Santos et al. (2023) and 99.65% by Sun et al. (2015). However, catalytic reactors have to operate at moderate temperatures as catalysts generally cannot withstand temperatures required to achieve a high degree of $CO_2$ conversion due to the quick deactivation caused by sintering (Tang et al., 2021). Even with catalysts characterized by good thermal stability and with sophisticated reactor designs, under realistic conditions, catalytic conversion usually does not exceed 50%; 36.3% was reported by Santos et al. (2023) and 49.7% by Sun et al. (2015). In addition, high residence times of reactants are required because of the relatively slow kinetics at moderate temperatures. This usually means that multiple passes through the reactor are needed to achieve a satisfactory conversion degree. Furthermore, the catalytic activity of catalysts tend to decrease over time, making the process less efficient, and the preparation of catalysts with desired characteristics might be costly. In the past, most research efforts have focused on catalyzed RWGS reactions. Currently, the main interest within catalyzed RWGS are:

1. mathematical modeling and design of a catalytic reactor (Ghodoosi et al., 2017; Benzinger et al., 2019; Santos et al., 2023),
2. development of inexpensive, synthetic catalysts with high selectivity, stability and activity at low temperatures [examples of such novel catalysts are molybdenum phosphide (Zhang et al., 2022), cerium oxide (Ebrahimi et al., 2022) or Ru clusters enclosed by silica shells (Tang et al., 2021)], and
3. technological advances to intensify the process and shift the chemical equilibrium towards CO by, e.g., in situ $H_2O$ removal (Desgagnés et al., 2024), application of an external electric field (Yamaoka et al., 2024), or combining the RWGS reaction with chemical looping (Pomiro et al., 2024).

The RWGS process can also be realized in a non-catalytic reactor fueled by a mixture of $CO_2$ and $H_2$. In such reactors, the temperature is not limited by the stability of the catalyst. Therefore, the reactors can be operated at elevated temperature, which greatly increases the conversion rate and shortens the residence time. The non-catalyzed alternative has not been much studied though. In the past, Bustamante et al. (2004) investigated the process in quartz and Inconel™ 600 reactors and formulated several global mechanisms for homogeneous RWGS reaction at different conditions. A novel non-catalyzed reactor concept was recently presented by Shekari et al. (2023), in which the RWGS reaction proceeds in a $H_2$ oxyflame, i.e., a flame resulting from feeding the reactor with streams of $H_2$ and $O_2$ + $CO_2$. At sufficiently high temperatures, conversion rates up to 79% were reported for impressively low residence times of the order of 0.01 s.

## 2. Numerical modeling

### 2.1. DNS versus LES

#### 2.1.1. Pencil code – the DNS solver

The DNS in this work are performed using the Pencil Code, which is a multi-purpose, high-order, open-source code (Pencil Code Collaboration et al., 2021). The continuity equation is given by

$$\frac{D\rho}{Dt} = -\rho\boldsymbol{\nabla}\cdot\boldsymbol{u}, \tag{3}$$

where $D/Dt = \partial/\partial t + \boldsymbol{u}\cdot\boldsymbol{\nabla}$ is the advective derivative, $\rho$ is the fluid density, and $\boldsymbol{u}$ is the velocity vector. The momentum equation reads

$$\frac{D\boldsymbol{u}}{Dt} = \frac{1}{\rho}\left(-\boldsymbol{\nabla}P + \boldsymbol{F}_{\text{vis}}\right), \tag{4}$$

where $P$ is the pressure and

$$\boldsymbol{F}_{\text{vis}} = \boldsymbol{\nabla}\cdot(2\rho\nu\, S) \tag{5}$$

is the viscous force with $S = \frac{1}{2}(\partial u_i/\partial x_j + \partial u_j/\partial x_i) - \frac{1}{3}\delta_{ij}\boldsymbol{\nabla}\cdot\boldsymbol{u}$ being the traceless rate-of-strain tensor and $\delta_{ij} = 1$ if $i = j$ and $\delta_{ij} =$

0 if $i \neq j$ is the Kronecker delta. The evolution of the mass fraction of species $k$ is given by

$$\frac{DY_k}{Dt} = -\frac{1}{\rho}\left(\boldsymbol{\nabla}\cdot\boldsymbol{J}_k + \dot{\omega}_k\right), \tag{6}$$

where $\boldsymbol{J}_k$ is the diffusive flux, which is calculated based on the mixture averaged approximation, and $\dot{\omega}_k$ is the reaction rate, both for species $k$. Finally, the energy equation is solved with respect to the logarithm of the temperature $T$ as

$$\frac{D\ln T}{Dt} = \frac{1}{c_p - R/m}\times \left[\sum_k \frac{DY_k}{Dt}\left(\frac{R}{m_k} - \frac{h_k}{T}\right) - \frac{R}{m}\boldsymbol{\nabla}\cdot\boldsymbol{u} + \frac{2\nu\, S^2}{T} - \frac{\boldsymbol{\nabla}\cdot\boldsymbol{q}}{\rho T}\right], \tag{7}$$

where $c_p$ is the heat capacity at constant pressure, $R$ is the universal gas constant, $m_k$ is the molar mass of species $k$, $m$ is the mean molar mass of the mixture,

$$\boldsymbol{q} = \sum_k h_k \boldsymbol{u} - \lambda\boldsymbol{\nabla}T \tag{8}$$

is the heat flux, $h_k$ is the enthalpy of species $k$, and $\lambda$ is thermal conductivity. Assuming an ideal gas, the pressure is found from

$$P = \frac{\rho RT}{m}. \tag{9}$$

For more details about the numerical implementation, the reader is referred to Babkovskaia et al. (2011). The chemical kinetic mechanism used here is the one of Li et al. (2015) with 14 species and 34 reactions.

#### 2.1.2. OpenFOAM – the LES solver

As for the Pencil Code, the LES solver consists of a coupled set of partial differential equations describing the transient evolution of multicomponent turbulent reacting flow. To reduce computational cost, the LES model does not resolve the smallest wavelengths, which in this work are removed using Favre-filtered balance equations for mass, momentum, and energy. The smallest scales are instead modeled using a dynamic one-equation subgrid-scale eddy viscosity model (Kim and Menon, 1995). The eddy viscosity model dynamically computes the filter coefficients appearing in the LES formulation. We use the open-source C++ libraries OpenFOAM-12. OpenFOAM is a generic platform for the finite-volume discretization of partial differential equations (Weller et al., 1998). The compressible reactive `reactingFoam` solver is used. Additionally, we employ the thermo-dynamically consistent `FickianTransportFoam` libraries provided by Rintanen and Morev (2025), appropriately accounting for non-unity Lewis number diffusivity effects. The Lewis number is defined as the ratio of thermal to mass diffusivity. This is particularly important for hydrogen-containing mixtures, such as those relevant for the RWGS, due to the large Lewis numbers of $H_2$ and H. These large Lewis numbers result in strong mass diffusion of the same species. The importance of correctly describing, e.g., enthalpy diffusion for $H_2$ flames in shear layer turbulence is emphasized by Cook (2009). Additionally, the `FickianTransportFoam` model allows to specify inter-species diffusion coefficients for a range of pressures and temperatures, which are consistently combined to provide the species' diffusion coefficient with respect to the mixture.

Turbulence-chemistry interaction is handled by the partially stirred reactor model (PaSR) (Fureby, 2012), assuming the chemical reactions to occur in topologically complex fine structures, making up a fraction of the volume in a given computational cell. Reaction rates are scaled by a correction factor $\kappa$ to tune the turbulence-chemistry interaction. In the PaSR formulation, this correction factor is estimated as

$$\kappa = \frac{\tau_c}{\tau_c + \tau_{\text{mix}}}, \tag{10}$$

where $\tau_c$ approximates the chemical timescale and $\tau_{\text{mix}}$ characterizes the turbulent mixing timescale. The chemical timescale is calculated from the elementary reaction rates in the chemical mechanism, while the turbulent mixing timescale is estimated based on characteristic turbulence quantities (Fureby, 2012). For the OpenFOAM implementation of the PaSR model, $\tau_{\text{mix}}$ depends linearly on the free parameter $C_{\text{mix}}$, i.e., $\tau_{\text{mix}} = C_{\text{mix}}\sqrt{\nu_{\text{eff}}/\epsilon}$, in terms of the effective turbulent viscosity, $\nu_{\text{eff}}$, and the turbulence dissipation rate, $\epsilon$. It can further be shown that

$$C_{\text{mix}} = \frac{1}{\sqrt{1 + 0.09\,\text{Re}}}, \tag{11}$$

in terms of the turbulent Reynolds number, Re. The coefficient $C_{\text{mix}}$ can be used to modulate the burning rate predicted by the PaSR model. Note that $C_{\text{mix}} = 0$ gives $\kappa = 1$, i.e., full reactivity of each computational cell. For the turbulence conditions at hand, $C_{\text{mix}} = 0.01$ is used. This is in line with previous work using the same computational setup for hydrogen combustion, e.g., Heggset et al. (2024b,a), Gruber et al. (2024), Meyer et al. (2026). The low sensitivity to the $C_{\text{mix}}$ parameter also for the present case is shown below (Section 3.3). The same detailed chemical reaction kinetics is used in the LES and the DNS.

In OpenFOAM, the PIMPLE algorithm, a hybrid SIMPLE-PISO iteration scheme, is used for pressure-velocity coupling, allowing an adaptive time step that is limited by the user-specified Courant number $\sim 0.9$. An implicit first order Euler scheme is used for time integration. Interpolation of the face fluxes to the cell values is achieved by combinations of second order central differencing schemes.

To sum up, the DNS and the LES models in this work are largely distinguished through the resolution of the smallest turbulent scales, the description of the turbulence-chemistry interaction, and the accuracy or order of the numerical schemes employed.

### 2.2. Some diagnostics measures

The mixture fraction based on $H_2$ for the streams used in this work, where the initial co-flow consist of only $H_2$ and $H_2O$ while there are no hydrogen containing species in the initial jet, is defined as

$$z_{\text{H}} = \frac{Z_{\text{H}}}{I_{\text{H}}}, \tag{12}$$

where

$$I_{\text{H}} = \frac{2m_{\text{H}}}{m_{\text{H}_2}}Y_{\text{init,H}_2} + \frac{2m_{\text{H}}}{m_{\text{H}_2\text{O}}}Y_{\text{init,H}_2\text{O}} \tag{13}$$

and

$$Z_H = \sum_{k=1}^{N_{\text{spec}}} Y_k \frac{\mu_{H,k} m_{\text{H}}}{m_k}. \tag{14}$$

In the above, $N_{\text{spec}}$ is the total number of species and $\mu_{H,k}$ is the number of hydrogen atoms in species $k$. In this way, $z_H$ is zero when there is no elemental hydrogen in the local gas, corresponding to the conditions of the initial central jet, and it is unity when the mixture equals the composition of the initial co-flow.

Another useful quantity that can be utilized to better understand non-premixed flames is the flame index (FI), which is able to distinguish between reactions that proceed in premixed and non-premixed modes. In particular, the flame index is negative when the gradients of the two reacting species have opposite directions, i.e., they are reacting before they have time to mix. This corresponds to a large Damköhler number. On the other hand, for a propagating flame that reacts in a premixed mode, i.e., the Damköhler number is small, the reactants are mixed before the combustion reaction is initiated by the high temperature of the flame front. In this situation, the gradients of the two reactants are in the same direction (away from the temperature-induced flame front) and the flame index is therefore positive. For the RWGS reaction, however, which, in contrast to the combustion reactions, is an endothermic reaction, there will be no temperature-induced flame front. Unlike for flames, the flame index will therefore be both positive and negative if the RWGS reaction proceeds under premixed conditions. For large Damköhler numbers, however, the flame index will be negative also for the RWGS reaction – just as it is for flames.

The jet mixture in this study consists of both $CO_2$ and $O_2$, which means that the flame index can be defined in two ways. The $O_2$-based flame index is defined as

$$\mathrm{FI}_{\mathrm{O}_2} = |\dot{\omega}_{\mathrm{O}_2}| \frac{\boldsymbol{\nabla} Y_{\mathrm{H}_2} \cdot \boldsymbol{\nabla} Y_{\mathrm{O}_2}}{|\boldsymbol{\nabla} Y_{\mathrm{H}_2}| \cdot |\boldsymbol{\nabla} Y_{\mathrm{O}_2}|}, \tag{15}$$

while the one based on $CO_2$ is given as

$$\mathrm{FI}_{\mathrm{CO}_2} = |\dot{\omega}_{\mathrm{CO}_2}| \frac{\boldsymbol{\nabla} Y_{\mathrm{H}_2} \cdot \boldsymbol{\nabla} Y_{\mathrm{CO}_2}}{|\boldsymbol{\nabla} Y_{\mathrm{H}_2}| \cdot |\boldsymbol{\nabla} Y_{\mathrm{CO}_2}|}. \tag{16}$$

Since the reactivity of $H_2$ with $O_2$ is very fast, this reaction will primarily proceed in a non-premixed mode. Because of this, and since the main reaction in this study is the reaction between $H_2$ and $CO_2$, we will in the following only consider the $CO_2$-based flame index as defined by Eq. (16).

### 2.3. Kinetic reaction mechanisms

Since only catalytic reactors are commercially available and the research focuses primarily on catalyzed RWGS reaction, a vast majority of chemical mechanisms were developed for the catalyzed RWGS reaction in different conditions and for different catalysts (Qi et al., 2020). They differ in complexity as the catalytic effect can be described by simple power law expressions, Langmuir-Hinshelwood type kinetics or intrinsic kinetics (Hernandez Lalinde et al., 2020; Wolf et al., 2016). Since the presence of catalysts affects the overall reaction rate, a different reaction mechanism is needed for each distinct catalyst, and for the same reason these mechanisms cannot be used to study uncatalyzed (homogeneous) RWGS reaction.

Several global mechanisms for uncatalyzed RWGS reaction were formulated in the past. A summary of those is given in Bustamante et al. (2004). All the global expressions are in the form of:

$$\frac{d[\mathrm{CO}]}{dt} = k[\mathrm{H}_2]^{1/2}[\mathrm{CO}_2], \tag{17}$$

where [ ] means concentration, $k = k_0 \exp(-E/RT)$ is the Arrhenius expression in which $k_0$ is the pre-exponential factor, $E$ is the activation energy, and $R$ and $T$ are the gas constant and temperature, respectively. The pre-exponential factor and activation energy are fitted to reproduce the experimental results, while the exponents for $H_2$ and $CO_2$ concentrations are derived based on the Bradford mechanism (Bradford, 1933):

$$\mathrm{H}_2 + M \Leftrightarrow 2\mathrm{H} + M, \tag{18}$$

$$\mathrm{H} + \mathrm{CO}_2 \Leftrightarrow \mathrm{CO} + \mathrm{OH}, \tag{19}$$

$$\mathrm{OH} + \mathrm{H}_2 \Leftrightarrow \mathrm{H}_2\mathrm{O} + \mathrm{H} \tag{20}$$

under the assumption of steady state for H and OH, and equilibrium for the $H_2$ di/re-association. The Bradford mechanism itself can also be used to describe RWGS reaction although no kinetic parameters are given in Bradford (1933) - the article in which the mechanism is introduced. A complete set of kinetic parameters for the Bradford mechanism was recommended by Kaskan & Browne (Kaskan and Browne, 1964) and their kinetic data for reactions 18–20 will in the following be referred to as the Bradford mechanism. It should be noted that the global expressions derived based on the Bradford mechanism have several limitations as they are strictly applicable only for low $CO_2$ conversion, and they are not consistent in a thermodynamical sense. Since in older experiments only a few percent of $CO_2$ conversion is reached, most often only coefficients for the forward reactions are provided. This means that the global expressions cannot predict a correct equilibrium composition, as will be shown in the next section.

There seems to be no detailed mechanisms developed specifically for the homogeneous RWGS reaction. However, many syngas combustion mechanisms are available, e.g. Kéromnès et al. (2013), Davis et al. (2005), Frassoldati et al. (2007), Li et al. (2015, 2022), Starik et al. (2010), Sun et al. (2007), and these should be suitable for modeling of $CO_2$ conversion via the RWGS reaction.

**Table 1**
Conditions relevant for the considered reactor.

| T [K] | P [Pa] | $X_{H_2}$ | $X_{H_2O}$ | $X_{CO_2}$ | $X_{CO}$ | $X_{N_2}$ | $X_{O_2}$ |
|---|---|---|---|---|---|---|---|
| 1650 | 3e6 | 0.5415 | 0.16 | 0.147 | 0.1385 | 0.0135 | 0.0 |

In order to gain confidence that the syngas mechanisms are appropriate for our purpose, their predictions should be compared with relevant experiments or, in the absence of complete dataset required for direct comparison (which is the case here), a comparison with global mechanisms formulated based on experimental results might be a viable alternative. First, we attempt to validate mechanisms by performing zero-dimensional (0D) simulations in Cantera (Goodwin et al., 2023) and comparing predictions of several syngas and global mechanisms. An attempt to reproduce experimental results of Graven & Long (Graven and Long, 1954) is also made. Next, implementation of the selected mechanisms into the Pencil Code is verified by comparison with Cantera tests. SI units are used for all results presented in this paper.

Four syngas combustion mechanisms of similar complexity are selected for zero dimensional tests: Kéromnès et al. (2013), Davis et al. (2005), Frassoldati et al. (2007) and Li et al. (2015). An isothermal and isobaric reactor available in Cantera was used for kinetics simulation with the selected mechanisms. The predictions were compared with five one-step global mechanisms specific for the RWGS reaction. The global mechanisms were formulated based on a few different sets of experimental results and are summarized by Bustamante et al. (2004).

For reference, results obtained using a more complex, widely-used mechanism for methane combustion, GRI 3.0, are also included in the study. Fig. 1 presents a comparison of global mechanisms and two selected detailed syngas mechanisms, while in Fig. 2 predictions of the other syngas mechanisms and GRI 3.0 are compared for the same conditions. As can be seen in Fig. 1, the discrepancy between global mechanism predictions is rather significant, they are therefore not a reliable source of validation data. Tingey (Tingey, 1966) associates this discrepancy with small, immeasurable amounts of $O_2$ that can have a great impact on the reaction rate - this effect will be further investigated later in this document. The detailed mechanisms are in the best agreement with the mechanisms formulated by Tingey (Tingey, 1966), at least for the studied conditions, which correspond to the conditions in which the experiment of Bustamante et al. (2004) was carried out ($T = 1200$ K, $P = 1$ bar and $CO_2/H_2 = 0.5/0.5$ (vol.)). Since the detailed mechanisms account for radicals formation, the predicted formation of $CO/H_2O$ and consumption of $H_2/CO_2$ is initially slower than what the global expressions predict. The mechanisms of Kéromnès et al. (2013), Davis et al. (2005) and Frassoldati et al. (2007) give very similar results to GRI 3.0, while the mechanism of Li et al. (2015) predicts slightly faster $CO_2$ conversion for the initial 50 seconds, as shown in Fig. 2. For the studied conditions, the Bradford mechanism (Bradford, 1933) is in a very good agreement with detailed syngas mechanisms.

Fig. 3 shows the same results obtained for the conditions listed in Table 1, which corresponds to typical industrial operating conditions. In these conditions, the conversion is several orders of magnitude faster due to higher temperature and pressure. All detailed mechanisms, and the Bradford mechanism, give, again, very similar results and converge towards the same equilibrium composition. The global expression is applicable only for the initial 0.01 seconds, after which it deviates significantly from the predictions of the detailed mechanisms due to the fact that the reaction progresses until all $CO_2$ is consumed, i.e. the global expression without the reverse reaction rate cannot predict the equilibrium state.

In an attempt to validate the syngas mechanisms against experimental data, a case corresponding to the experiment performed by Graven & Long (Graven and Long, 1954) was set up. In the experiment a stream of $H_2$, $CO_2$ and $N_2$ was introduced into a cylindrical quartz reactor. The $CO_2$ partial pressure was kept constant, while the $H_2$ flow rate was var-

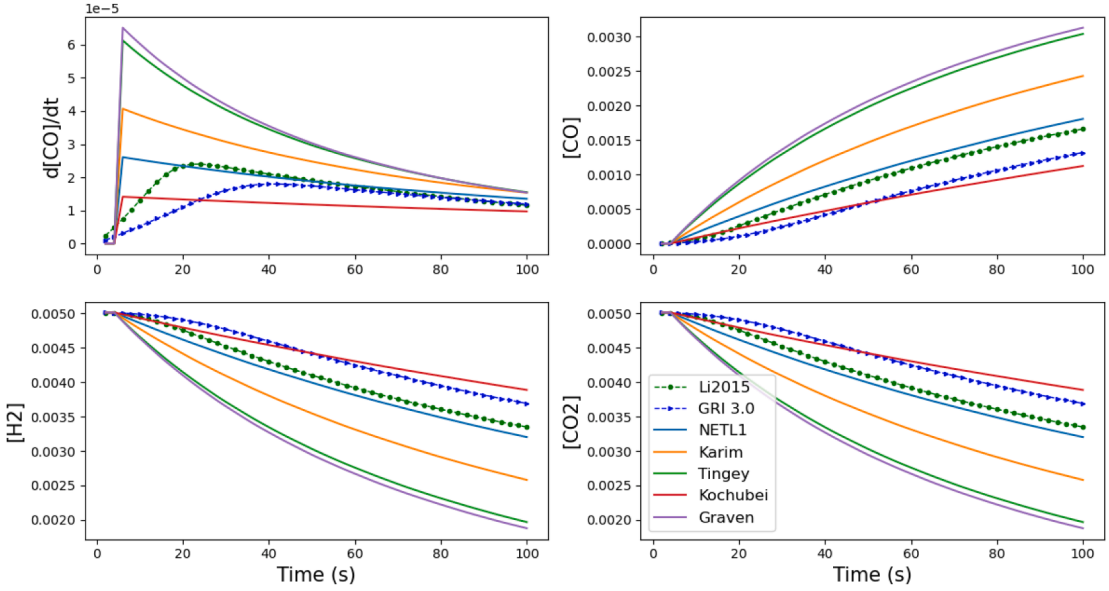


**Fig. 1.** Comparison of species concentrations (kmol/m$^3$) for global and selected detailed mechanisms in conditions corresponding to experiment of Bustamante et al. (2004). The two detailed mechanisms are marked with green and blue symbols.

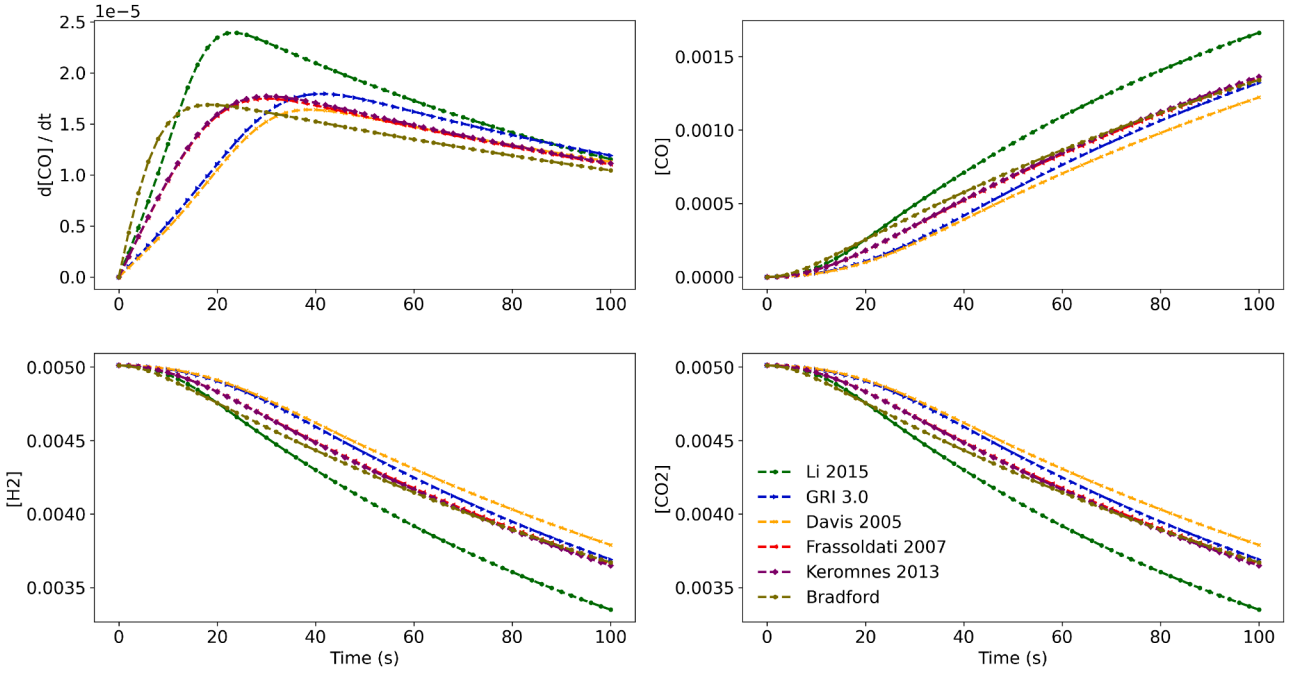


**Fig. 2.** Comparison of syngas mechanisms predictions of species concentrations (kmol/m$^3$) in conditions corresponding to experiment of Bustamante et al. (2004).

ied. The total pressure was kept constant by adjusting the $N_2$ flow rate. The temperature inside the reactor was kept constant at 1173 K and the composition was measured at the reactor outlet after a flow time of 0.53 s. The results are presented in Fig. 4 in the form of the resulting $H_2O$ partial pressure (as computed after 0.53 s) as a function of inlet $H_2$ partial pressure. The authors of the experiment claim that the reacting mixture was completely purified from $O_2$. If this is truly the case, the results obtained using all tested syngas mechanisms differ by 3 orders of magnitude from the experimental data (solid lines in Fig. 4 corresponding to $X_{O_2} = 0.0$). However, if the measurements of the $O_2$ fraction were less accurate than six significant digits, then it is very likely that trace amounts of $O_2$ were present in the reactor. These small amounts of $O_2$ could have a significant impact on the results, as can be seen in Fig. 4 for the cases with $X_{O_2} = 2.5{\cdot}10^{-6}$ (dashed lines) and $X_{O_2} = 5{\cdot}10^{-6}$ (dotted lines). In fact, Graven & Long claimed that 1% of $O_2$ in the mixture accelerated the reaction 100-fold – it is indeed predicted by all syngas mechanisms that the reaction rate becomes 20–800 times faster (depending on the initial $H_2$ partial pressure and mechanism) when the $O_2$ fraction increases from $2.5{\cdot}10^{-6}$ to $1{\cdot}10^{-2}$. It should be noted that the mechanism of Bradford (Bradford, 1933) was excluded from considerations in Fig. 4 as it does not include $O_2$, and therefore cannot account for the effect of $O_2$ on the reaction rate.

By analyzing the net progress rates of reactions and species fractions at the end of simulation for the cases in which $X_{O_2} = 0$ and $X_{O_2} = 2.5{\cdot}10^{-6}$, the strong effect that small amounts of $O_2$ has on the reaction will be explained in the following.

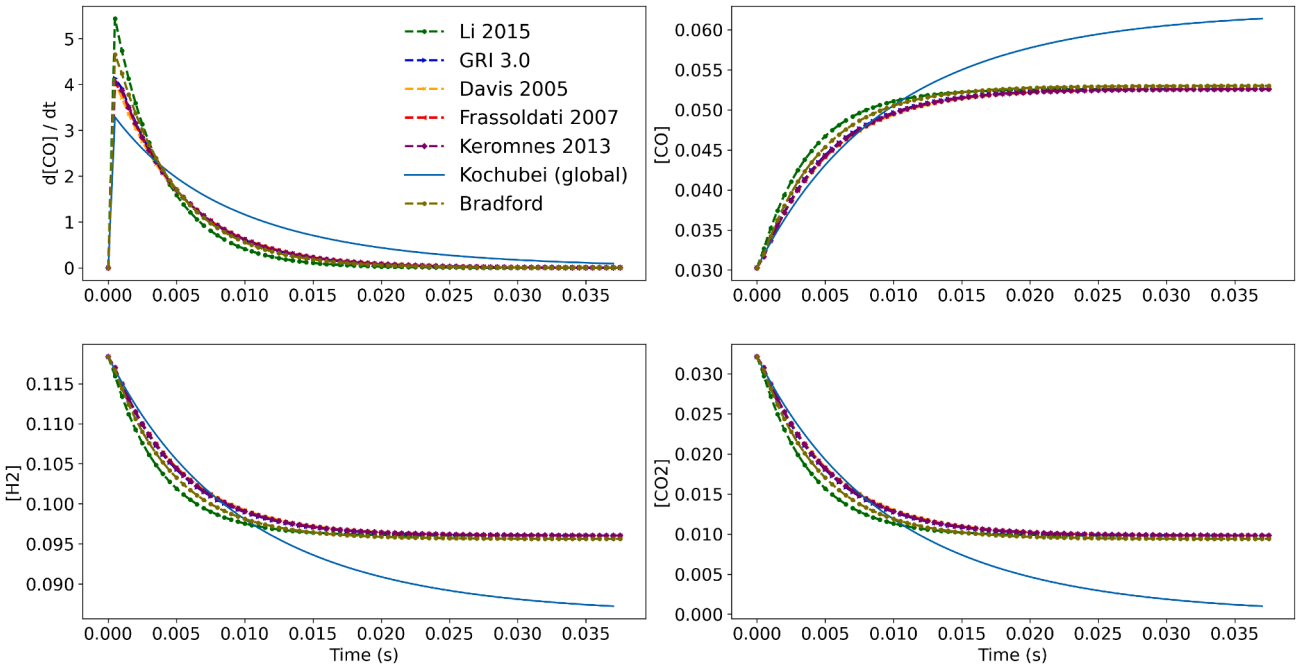


**Fig. 3.** Comparison of selected mechanisms predictions of species concentrations (kmol/m$^3$) in conditions relevant for the studied reactor.

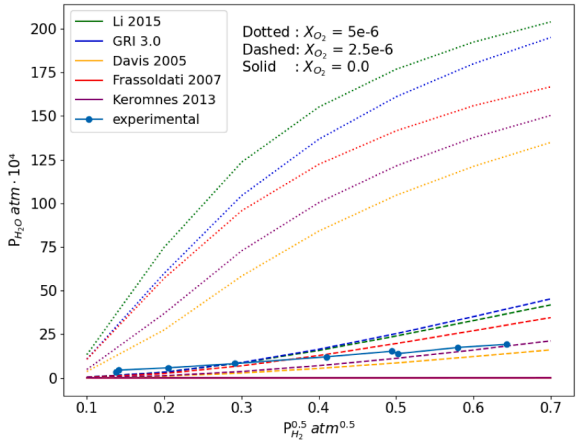


**Fig. 4.** Predictions of syngas mechanisms for the conditions corresponding to the experiment of Graven & Long (Graven and Long, 1954).

The presence of $O_2$ causes much quicker formation of the OH radical, especially through the reaction

$$H + O_2 \Leftrightarrow O + OH. \quad (21)$$

This reaction does not happen when $X_{O_2} = 0$ but it is among the fastest progressing reactions when $X_{O_2} = 2.5{\cdot}10^{-6}$. Additionally, substantial amounts of OH are produced through reactions of H, $H_2$, $H_2O$, $HO_2$ with atomic oxygen radical (O), produced from $O_2$ dissociation. As a result, in the presence of $O_2$, the concentration of the OH radical is much higher - about 3–4 orders of magnitude in the considered case - than for the case with $X_{O_2} = 0$. Subsequently, the fastest of all reactions,

$$H_2 + OH \Leftrightarrow H + H_2O, \quad (22)$$

progresses a few orders of magnitude faster when $O_2$ is present in the mixture. The atomic hydrogen radical (H) is then consumed according to the reverse of reaction

$$CO + OH \Leftrightarrow CO_2 + H, \quad (23)$$

the net rate of progress of which is almost equal to the negative of the net rate of progress of reaction (22). Apart from CO, more OH radical is produced through reaction (23), which in turn accelerates reaction (22). Based on the potentially strong effect that even very small amounts of $O_2$ have on the reaction rate, it is tempting to call it a catalytic effect, but this is not appropriate since the $O_2$ is actually consumed in the process. Instead, we call it the oxygen derived free-radical promoted effect.

To quantify the role of these three elementary reactions (Eqs. (21)–(23)), a brute-force sensitivity analysis was performed in Cantera using the Li et al. (2015) mechanism for the Graven & Long conditions of Fig. 4 ($T = 1173$ K, $P = 1$ atm, $t = 0.53$ s). For every elementary reaction $j$ in the mechanism, the normalised sensitivity coefficient $S_{ij} = d \ln X_i / d \ln k_j$ is computed for both target species $X_{CO}$ and $X_{OH}$. To remove the directional ambiguity that affects sensitivity bars of reversible reactions (whose $k_f$ controls both forward and reverse rates through detailed balance), each sensitivity coefficient is paired with the signed net rate of progress $q_{\text{net},j}$ of the same reaction at the same evaluation time, following the workflow recommended in Turányi and Tomlin (2014). The results are summarised in Fig. 5. With $X_{O_2} = 2.5{\cdot}10^{-6}$, the three reactions (21) and (23) are confirmed to be by far the dominant sensitivities for both targets: $H + O_2 \leftrightarrow O + OH$ yields $S_{CO} \approx +2.4$ and $S_{OH} \approx +2.8$, while $H_2 + OH \leftrightarrow H + H_2O$ has $S_{OH} \approx -1.0$ (chain-propagation step that consumes OH but regenerates H). Removing the $O_2$ from the mixture eliminates the $H + O_2 \leftrightarrow O + OH$ sensitivity entirely and leaves the slow $2H + M \leftrightarrow H_2 + M$ three-body recombination as the rate-limiting step, in agreement with the qualitative Bradford-mechanism picture (Bradford, 1933; Kaskan and Browne, 1964). The signed $q_{\text{net}}$ values in the right column of Fig. 5 further show that, at these conditions, the reaction $CO + OH \leftrightarrow CO_2 + H$ is net running right-to-left, i.e. it is a net CO producer despite being written with CO on the reactant side – consistent with its large positive sensitivity for $X_{CO}$.

The mechanistic claim that CO production is OH-limited can also be tested quantitatively. Fig. 6 shows the instantaneous net CO molar production rate $\dot{\omega}_{CO}$ as a function of the local [OH] from a sweep of isothermal-isobaric 0D simulations spanning $10^{-6} \le X_{O_2,0} \le 10^{-1}$ at $T = 1650$ K. Over the active phase of the reaction the trajectories collapse onto a slope-one curve in both pressure panels, demonstrating that

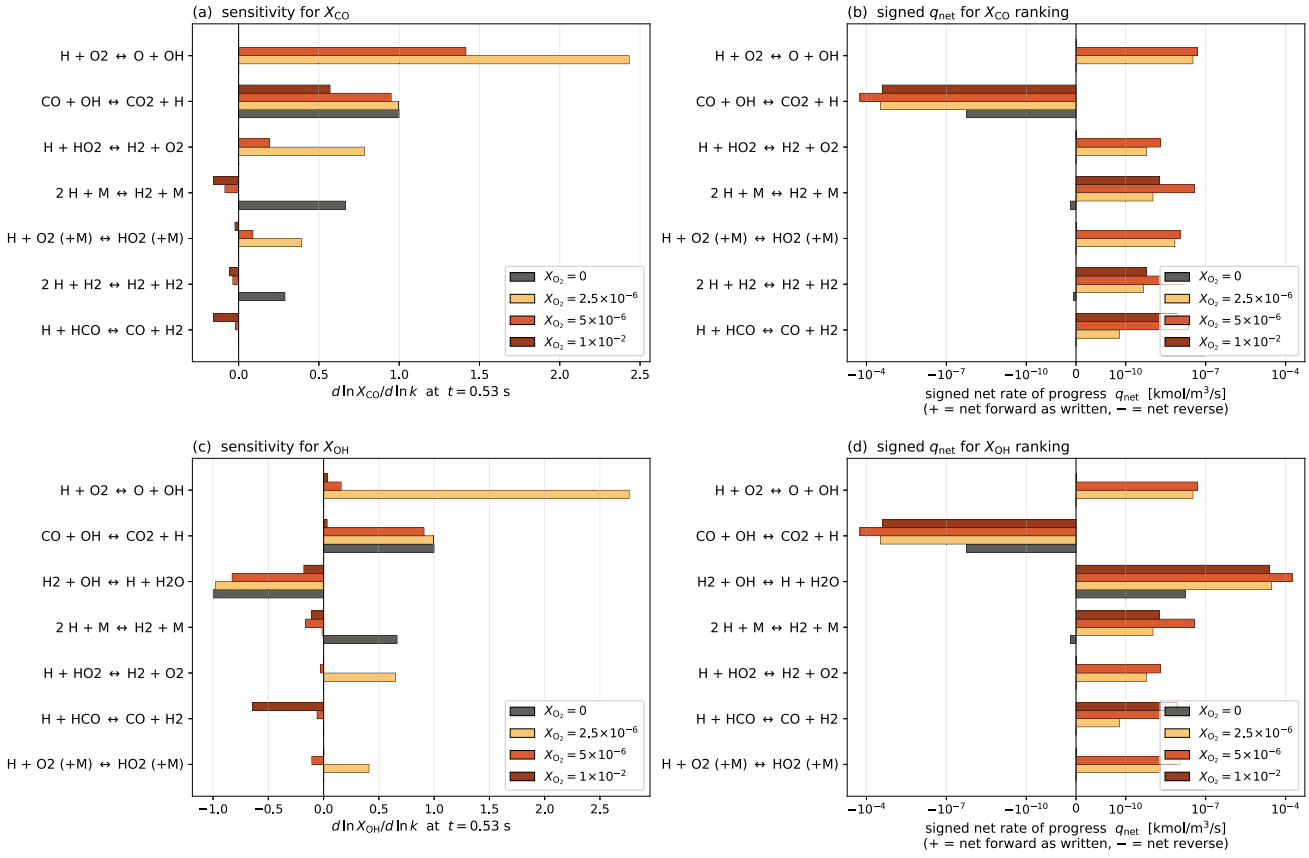


**Fig. 5.** Sensitivity of $X_{CO}$ (top row, panels a–b) and of $X_{OH}$ (bottom row, panels c–d), each paired with the signed net rate of progress $q_{net}$ of the same reaction, for the seven most sensitive reactions at the Graven & Long conditions ($T = 1173$ K, $P = 1$ atm, $t = 0.53$ s) and four initial $O_2$ levels (colour scale). Sensitivity coefficients are normalised, $S_{ij} = d\ln X_i/d\ln k_j$; positive (negative) $q_{net}$ values indicate that the reaction is net running in the forward (reverse) direction as written. The pairing removes the directional ambiguity of sensitivity coefficients of reversible reactions, in line with the recommendation of Turányi and Tomlin (2014).

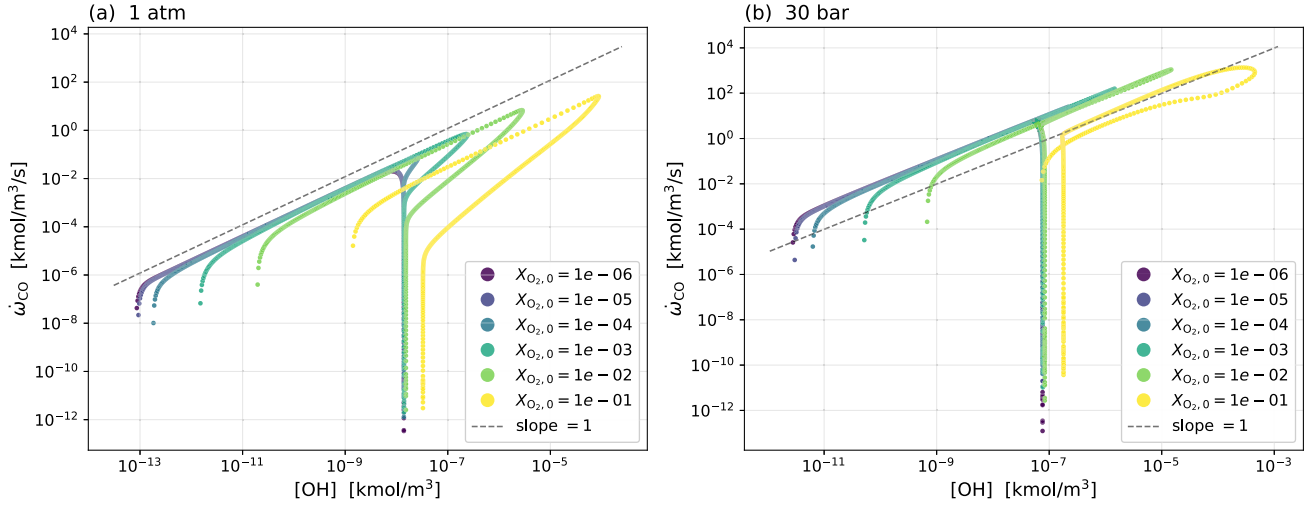


**Fig. 6.** Instantaneous net CO molar production rate $\dot{\omega}_{CO}$ against local OH concentration [OH], from a sweep of initial $O_2$ mole fractions (colour scale) in isothermal-isobaric 0D simulations at $T = 1650$ K. The dashed black line shows a slope of 1 for reference; in both pressure panels the active phase of every trajectory tracks this slope, confirming that $\dot{\omega}_{CO} \propto$ [OH] at fixed temperature.

at fixed temperature $\dot{\omega}_{CO} \propto$ [OH], i.e. the CO production rate is set by the available amount of H through reaction (23), with H regenerated from OH by reaction (22) in quasi-steady-state. I.e.; trace amounts of $O_2$ accelerate CO production primarily by raising the OH level via reaction (21), not by introducing a new CO-producing pathway.

The free-radical promoted effect of $O_2$ makes validation of the selected mechanisms very challenging. Only experiments with extremely accurate measurements of $O_2$ fraction provide useful data for validation and the accuracy of such measurements is rarely stated. The quantitative $O_2$ scaling presented later in this paper (Fig. 9) shows that an inlet

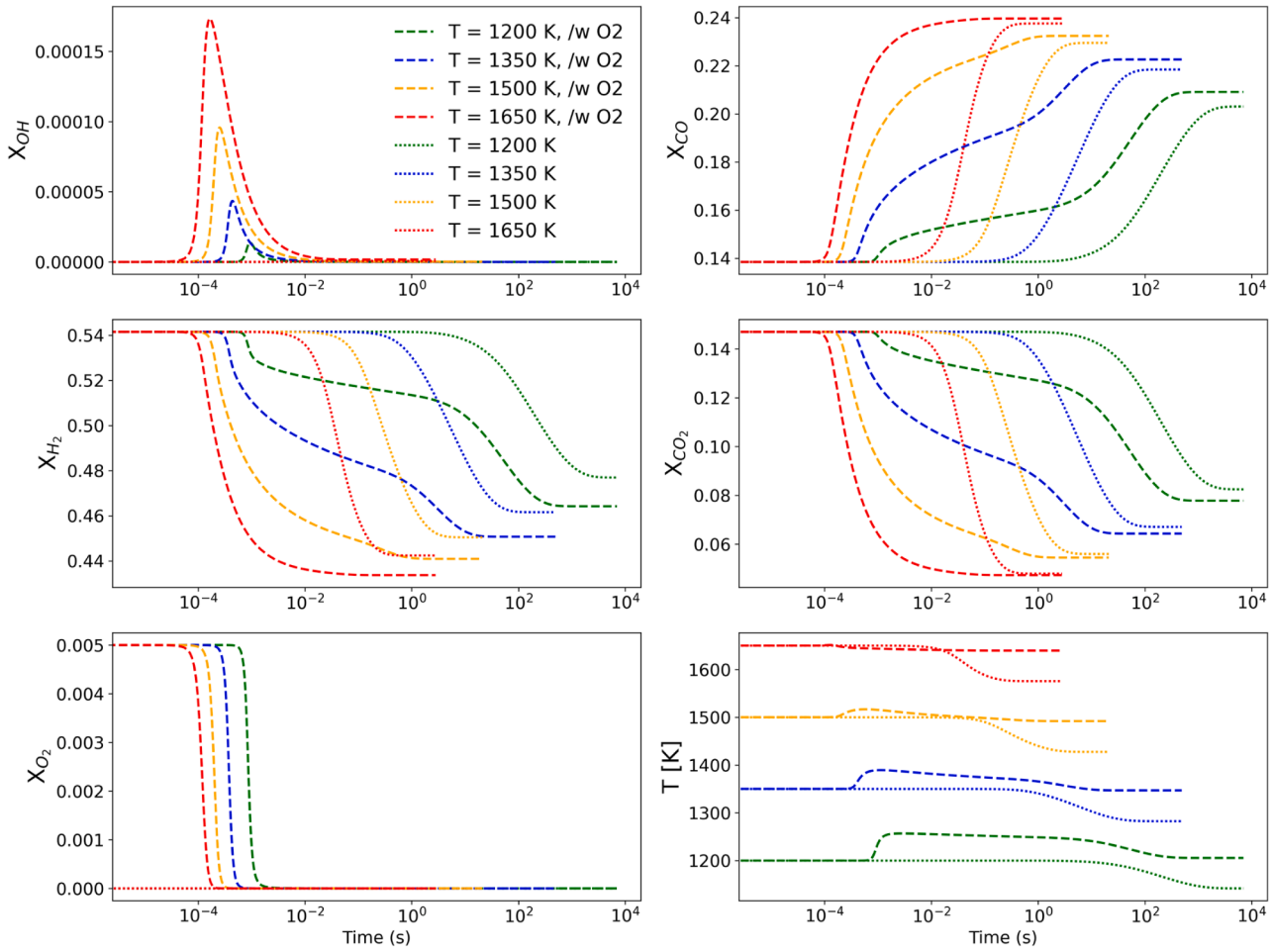


**Fig. 7.** Effect of 0.5% volumetric $O_2$ content at atmospheric pressure.

$O_2$ mole fraction of order $10^{-6}$ is already sufficient to change the conversion time by an order of magnitude, which sets the accuracy floor that any experimental campaign aiming to validate these mechanisms must meet. As we are unaware of experimental results with the required accuracy for $O_2$ concentration measurements, it seems reasonable to trust that the well-known and widely-used mechanisms optimized for syngas combustion are also suitable for modeling of the RWGS reaction. Since the predictions of all detailed mechanisms are similar, and given that the stiffness of the mechanisms is also similar, it is reasonable to choose the one with the lowest number of species and reactions as it will minimize the computational cost of the resolved simulations. The number of species and reactions for the selected syngas mechanisms, as well as the time step required due to mechanism stiffness, are shown in Table 2, from which it can be concluded that it will be computationally least expensive to employ the mechanisms of Li et al. (2015) or Davis et al. (2005). However, if the free-radical promoted effect of $O_2$ is insignificant, and a real reaction pathway is not of interest, it will by far be cheapest to use the mechanism of Bradford (Bradford, 1933; Kaskan and Browne, 1964). For the rest of this paper, unless otherwise specified, we will use the mechanism of Li et al.

## 3. Results

### 3.1. Premixed zero-dimensional simulations

The increased rate of the RWGS reaction due to the presence of trace amount $O_2$ might be very beneficial for the reactor performance as much faster conversion means much shorter residence times, which can reduce the overall size of the reactor. In order to explore potential benefits of the free-radical promoted effect of $O_2$, additional zero-dimensional simulations are performed in Cantera. This time, only one mechanism, the mechanism of Davis et al. (2005), is used, and the simulations are performed for temperatures that are likely to occur in the reactor, ranging from 1200 to 1650 K. The composition is the same as given in Table 1, with a difference that in half of the cases 0.5% of $N_2$ is replaced by $O_2$. Simulations are performed both at atmospheric pressure and at 30 bar, to get a sense for how important the effect of $O_2$ is in the conditions of interest (the reactor is planned to be operated at high pressure) relative to the atmospheric pressure at which the experiment of Graven & Long (Graven and Long, 1954) was performed. Fig. 7 presents the results for atmospheric pressure, while Fig. 8 presents the same results for high pressure. In the figures the cases with no $O_2$ are marked by dotted lines, while the cases with 0.5% volumetric $O_2$ content are marked by dashed lines.

As can be seen in Fig. 7, the effect of added $O_2$ at atmospheric pressure is strongest for highest temperature, $T = 1650$ K, at which the equilibrium state is reached around two orders of magnitude faster in the presence of $O_2$, compared to the cases without $O_2$. For lower temperatures, conversion for the cases with $O_2$ begins about three orders of magnitude faster than without $O_2$, but the speed-up in the total conversion, at which the equilibrium state is reached, is not as large. The most likely reason for that is that for higher temperatures much more OH radicals is produced (see upper left panel of Fig. 7), which sustains faster conversion rate for the entire conversion duration. For cases with

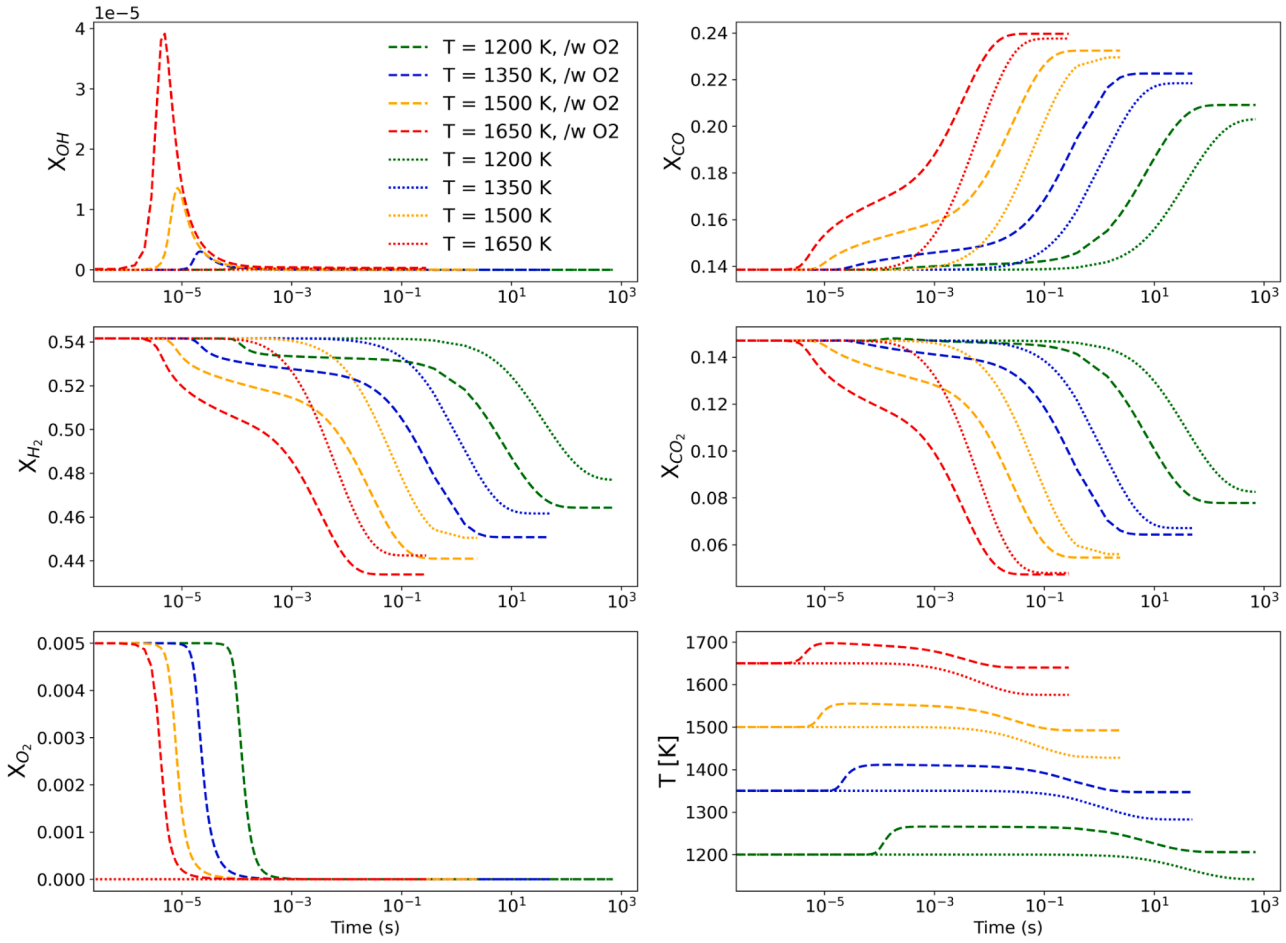


**Fig. 8.** Effect of 0.5% volumetric $O_2$ content at 30 bar.

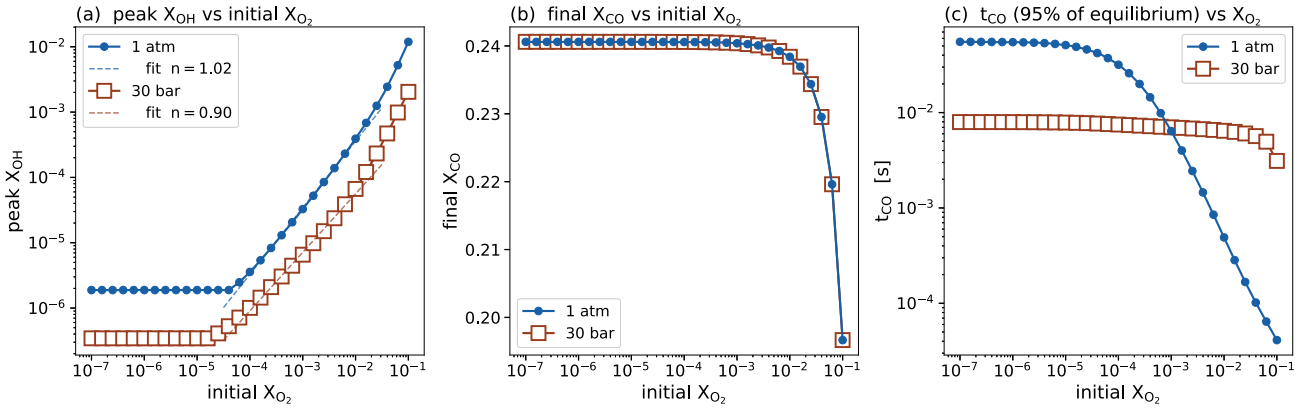


**Fig. 9.** Initial-$O_2$ scaling at the reactor conditions of Table 1 ($T$ = 1650 K, balance via $H_2$): (a) peak $X_{OH}$ vs. initial $X_{O_2}$, with the fitted power law $X_{OH,peak} \propto X_{O_2}^n$ overlaid for both pressures; (b) final $X_{CO}$; (c) time $t_{CO}$ required to reach 95% of the equilibrium CO yield. Isothermal-isobaric 0D simulations using the Li et al. (2015) mechanism.

**Table 2**
Number of species and reactions for the selected mechanisms.

| Mechanism | Number of species | Number or reactions | Required time step |
|---|---|---|---|
| Li et al. (2015) | 14 | 37 | 2e-9 |
| Davis et al. (2005) | 14 | 38 | 2e-9 |
| Kéromnès et al. (2013) | 15 | 48 | ND |
| Frassoldati et al. (2007) | 21 | 62 | ND |
| GRI 3.0 | 53 | 325 | 2e-9 |
| Bradford (Bradford, 1933; Kaskan and Browne, 1964) | 6 | 3 | 1e-9 |

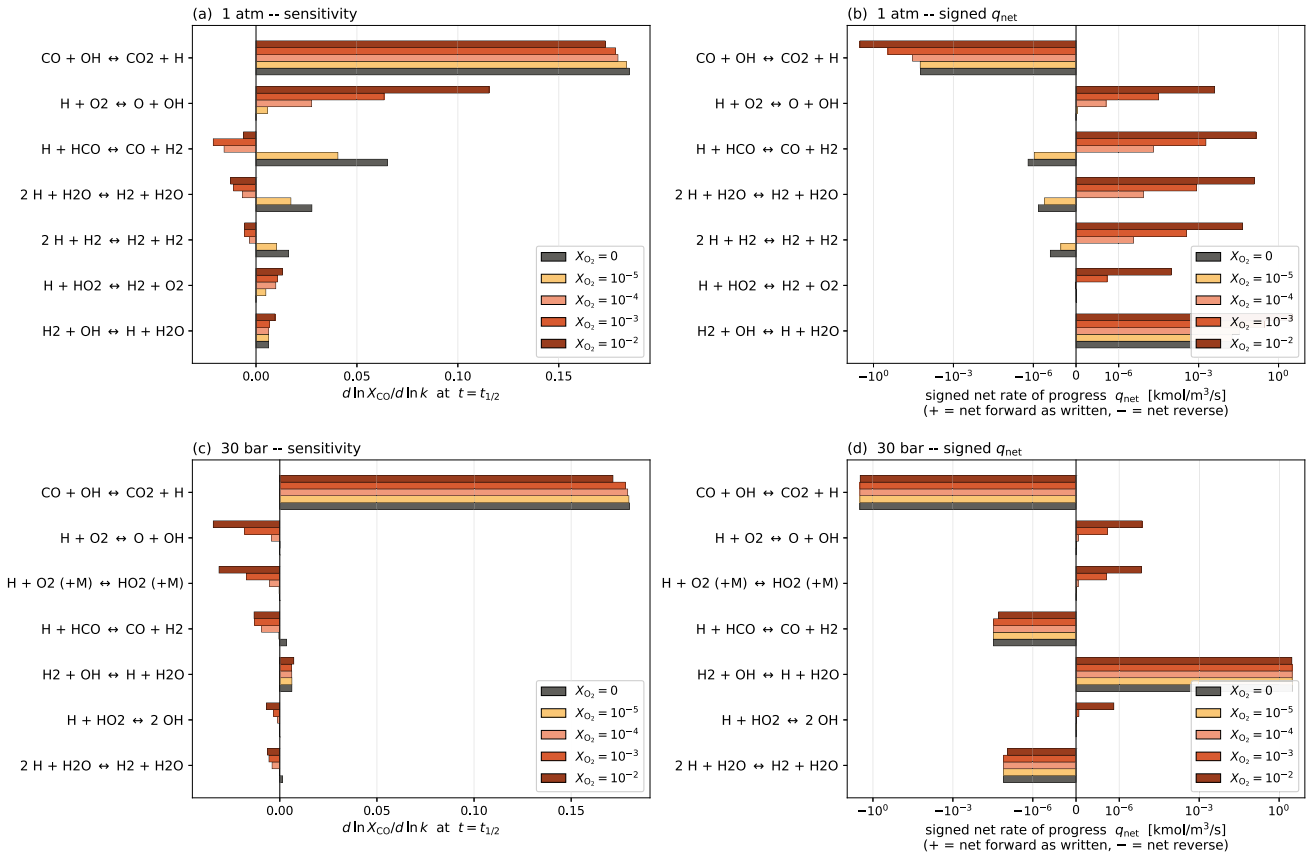


**Fig. 10.** Sensitivity of $X_{CO}$ (panels a, c) paired with the signed net rate of progress $q_{net}$ (panels b, d) for every reaction in the top of the sensitivity ranking, at the reactor conditions of Table 1 ($T = 1650$ K) and for five initial $O_2$ levels (colour scale). Top row: 1 atm; bottom row: 30 bar. Sensitivities are evaluated at the time at which $X_{CO}$ reaches half of its equilibrium value, so the four $O_2$ cases are compared at the same conversion fraction. Positive (negative) $q_{net}$ values indicate that the reaction is net running in the forward (reverse) direction as written. The pairing removes the directional ambiguity of sensitivity coefficients of reversible reactions, in line with the recommendation of Turányi and Tomlin (2014).

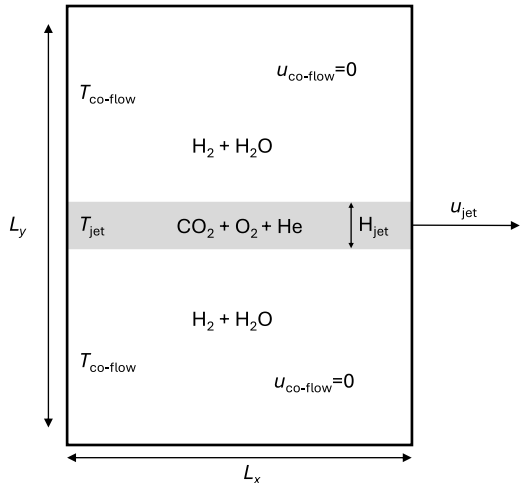


**Fig. 11.** Sketch of initial condition for the temporal jet setup.

lower temperatures, the conversion rate decreases when OH radicals are consumed after around 0.001 - 0.01 s, which can be seen as flattening of the conversion curves for CO, $H_2$ and $CO_2$.

Looking now at the corresponding results for the cases with higher pressure in Fig. 8, it is clear that the free-radical promoted effect of $O_2$ is weaker than at atmospheric pressure. At this pressure, however, the effect of $O_2$ is much less dependent on temperature, and the effect is strongest for lowest temperature, at which the equilibrium state is reached about one order of magnitude earlier in the presence of $O_2$. This change is probably due to significantly smaller amount of OH radicals that are created at high pressure. In conclusion, for the range of temperatures that are likely to be present in the considered reactor, the free-radical promoted effect of $O_2$ in high-pressure conditions is expected to be weaker than at atmospheric pressure. Nevertheless, the effect is still significant and has the potential to benefit the reactor performance.

To make the above pressure-dependent statement quantitative, an initial-$O_2$ sweep was performed at the reactor conditions of Table 1, i.e. $T = 1650$ K and the same baseline composition, with $O_2$ substituted for $H_2$ over the range $10^{-7} \le X_{O_2} \le 10^{-1}$. The simulations are isothermal-isobaric 0D runs using the Li et al. (2015) mechanism, performed at both $P = 1$ atm and $P = 30$ bar. Three derived quantities are extracted: the peak $X_{OH}$ reached during the integration, the final $X_{CO}$, and the time $t_{CO}$ to reach 95% of the equilibrium CO yield. The results are summarised in Fig. 9. In the active scaling regime, $10^{-4} \lesssim X_{O_2} \lesssim 10^{-2}$, the peak OH scales as a power law $X_{OH,peak} \propto X_{O_2}^{n}$ with $n \approx 1.0$ at 1 atm and $n \approx 0.9$ at 30 bar. The exponents are nearly the same at both pressures, but the absolute level of the OH curve at 30 bar lies a factor of ~5–6 below the 1 atm curve, so the trace-$O_2$ effect on $t_{CO}$ is correspondingly weaker at the higher pressure (panel c): $t_{CO}$ drops by about three decades at 1 atm but by only a factor of ~3 at 30 bar over the same $O_2$ range. Below $X_{O_2} \approx 4 \cdot 10^{-5}$ at 1 atm and $\approx 2 \cdot 10^{-5}$ at 30 bar, the OH pool is set by the thermal $H_2/H_2O/CO_2/CO$ chemistry alone and is insensitive

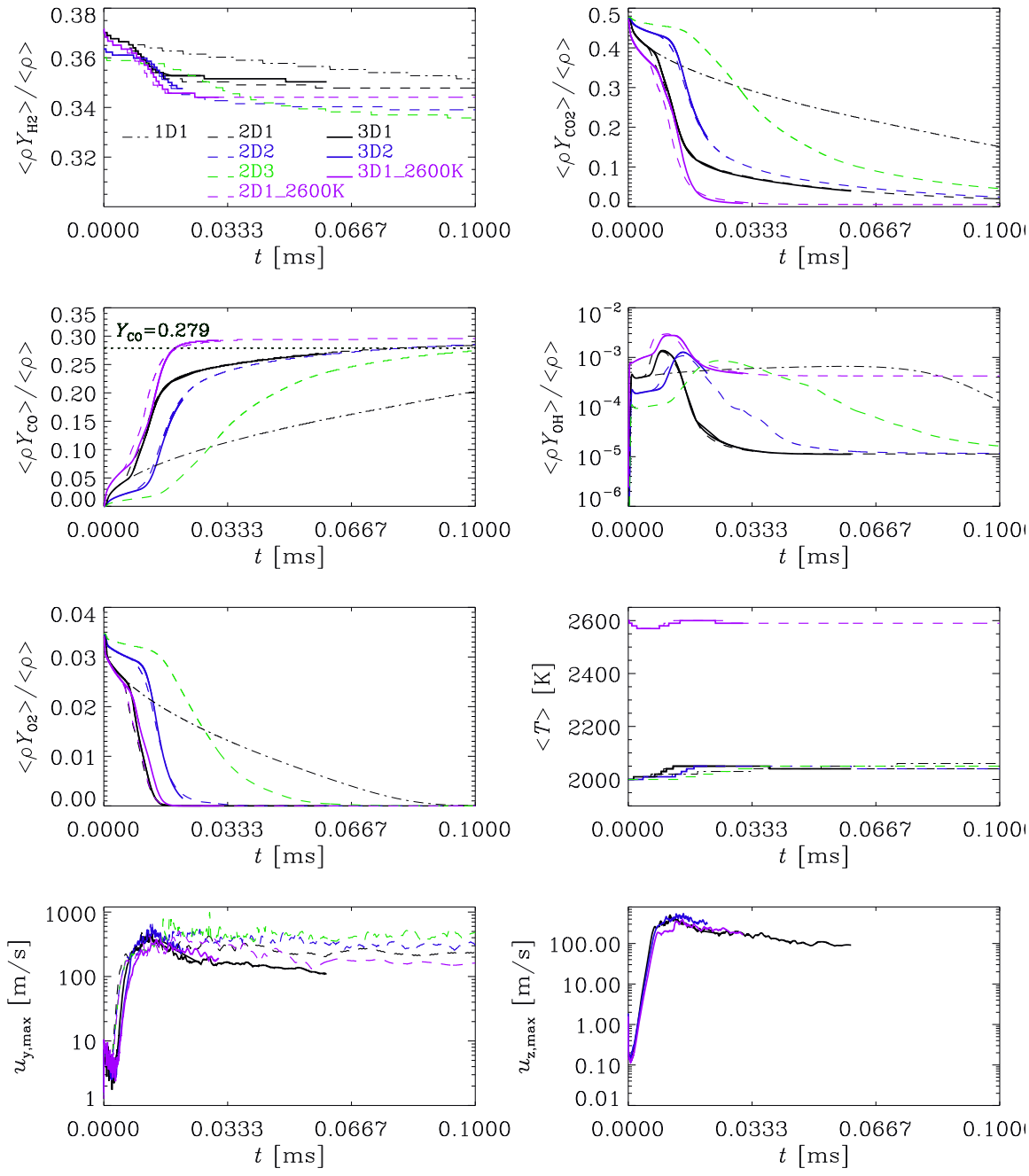


**Fig. 12.** Results for some of the temporal jet simulations defined in Tables 3 and 4.

to the trace-$O_2$ level; this provides a quantitative threshold below which the radical-promoted effect is negligible at reactor temperatures. The final CO yield (panel b) is independent of $O_2$ below a few percent and drops only when the added $O_2$ consumes a significant fraction of the available $H_2$.

The change in the trace-$O_2$ effect with pressure can be explained quantitatively by repeating the sensitivity analysis of Section 2.3 at the reactor conditions and pairing each sensitivity bar with the corresponding signed net rate of progress, see Fig. 10. The dominant positive sensitivity for $X_{CO}$ is the same at both pressures and across all $O_2$ levels: CO + OH ↔ $CO_2$ + H with $S_{CO} \approx +0.18$, and the corresponding $q_{net}$ is negative at all conditions tested, confirming that this reaction is net running right-to-left and is by far the dominant CO source. What differs between the two pressures is the secondary sensitivity. At 1 atm, the chain-branching reaction H + $O_2$ ↔ O + OH has a sensitivity for $X_{CO}$ that grows from zero at $X_{O_2} = 0$ to +0.12 at $X_{O_2} = 10^{-2}$, and its $q_{net}$ is strongly positive (forward, generating OH). At 30 bar, the same reaction has a sensitivity that is at most marginal, and is actually negative for finite $O_2$; the three-body recombination H + $O_2$(+M)↔ $HO_2$(+M) appears in its place with a comparable $q_{net}$ that is also positive (forward) but corresponds to chain termination via the relatively unreactive $HO_2$ product. The interpretation is therefore that: at elevated pressure the three-body recombination outcompetes the chain branching, so $O_2$ molecules end up removing H atoms at roughly the same speed as they add OH to the chain. In addition, the chain branching reaction, H + $O_2$ ↔ O + OH, has a negative CO-sensitivity.

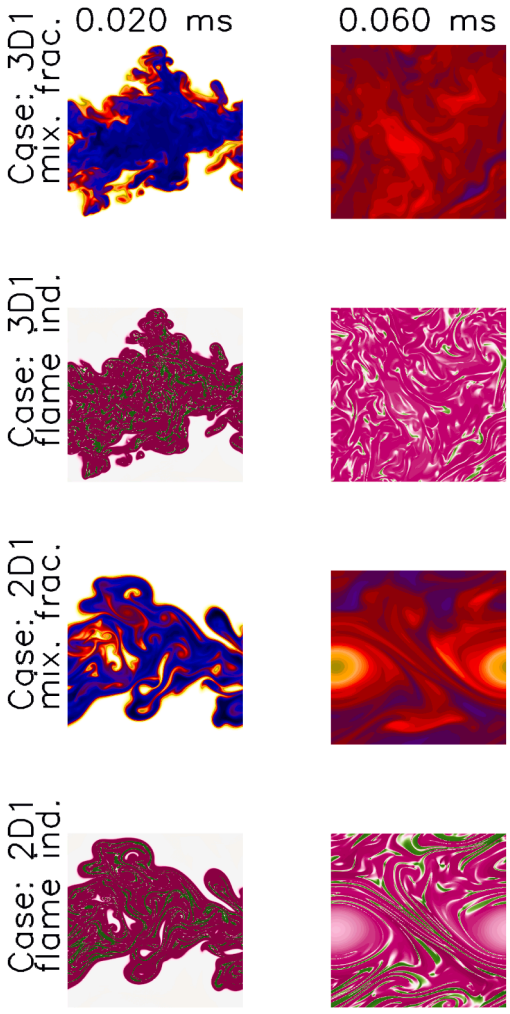


**Fig. 13.** Cross sections of mixture fraction (rows 1 and 3) and flame index (rows 2 and 4) for early (left column) and late (right column) times. Results from three-dimensional simulations are shown in the two upper rows, while results from two-dimensional simulations are shown in the two last rows.

### 3.2. Temporal jet simulations

The aim of this work is to investigate the coupling between mixing and the endothermic RWGS reaction. For simplicity and computational efficiency, the temporal jet framework (Hawkes et al., 2007), as presented in Fig. 11, will be utilized to study the effect of turbulence on the RWGS reaction. The initial conditions are homogeneous in the third direction, which has an extent of $L_z$. All boundary conditions are periodic.

It should be noted that the velocity jet ($H_{\text{jet},u}$) is slightly thinner than the scalar (temperature and species) jet ($H_{\text{jet,sc}}$). This has been done to avoid numerical problems due to the strong difference in viscosity and density between $H_2$ and $CO_2$. Another modification that has been done to alleviate this problem is to add some helium to the $CO_2$ stream. The helium does not have any impact on the reactions, but it increases the viscosity and lowers the density of the jet to make it more similar to that of the $H_2$-dominated co-flow. All simulations are performed for a pressure of 30 bar. To study the effect of turbulence on the RWGS reaction, the Damköhler number, given by the ratio of the fluid and chemical timescales, must be significantly smaller than unity. The Damköhler number is defined as

$$\text{Da} = \frac{\tau_\text{f}}{\tau_\text{c}}, \tag{24}$$

**Table 3**
Dimensions and initial parameters for the various simulations. In addition to what is listed in the table, all simulations have the following in common; the initial thickness of the shear layer is given by $\delta_{\text{shear}} = 0.02$ mm, which is smoothed with a hyperbolic profile between the jet and the co-flow, the mesh size, which is the same in all directions, is $\Delta x = 4 \times 10^{-3}$ mm, the velocity of the jet is $u_{\text{jet}} = 387.5$ m/s, the mass fraction of helium is 0.2 in the jet and zero in the co-flow, the mass fraction of steam is zero in the jet and 0.001 in the co-flow while the mass fraction of $H_2$ is 0 in the jet and 0.999 in the co-flow.

| | Dimensions | | | Jet | | | | Co-flow |
|---|---|---|---|---|---|---|---|---|
| Case | $H_{\text{jet},u}$ [mm] | $H_{\text{jet,sc}}$ [mm] | $L_x, L_y, L_z$ [mm] | $T_{\text{jet}}$ [K] | $Y_{O_2}$ – | $Y_{N_2}$ – | $Y_{CO_2}$ – | $T_{\text{co-flow}}$ [K] |
| One-dimensional simulations | | | | | | | | |
| 1D1 | 0.134 | 0.2 | –, 2, – | 2000 | 0.054 | 0 | 0.746 | 2000 |
| 1D2 | 0.268 | 0.4 | –, 4, – | 2000 | 0.054 | 0 | 0.746 | 2000 |
| 1D1noO2 | 0.134 | 0.2 | –, 2, – | 2000 | 0 | 0.054 | 0.746 | 2000 |
| Two-dimensional simulations | | | | | | | | |
| 2D1 | 0.134 | 0.2 | 2, 2, – | 2000 | 0.054 | 0 | 0.746 | 2000 |
| 2D2 | 0.268 | 0.4 | 4, 4, – | 2000 | 0.054 | 0 | 0.746 | 2000 |
| 2D3 | 0.536 | 0.8 | 8, 8, – | 2000 | 0.054 | 0 | 0.746 | 2000 |
| 2D1noO2 | 0.134 | 0.2 | 2, 2, – | 2000 | 0 | 0.054 | 0.746 | 2000 |
| 2D1x2O2 | 0.134 | 0.2 | 2, 2, – | 2000 | 0 | 0.108 | 0.692 | 2000 |
| 2D1-1800K | 0.134 | 0.2 | 2, 2, – | 1800 | 0.054 | 0 | 0.746 | 1800 |
| 2D1-2200K | 0.134 | 0.2 | 2, 2, – | 2200 | 0.054 | 0 | 0.746 | 2200 |
| 2D1-2400K | 0.134 | 0.2 | 2, 2, – | 2400 | 0.054 | 0 | 0.746 | 2400 |
| 2D1-2600K | 0.134 | 0.2 | 2, 2, – | 2600 | 0.054 | 0 | 0.746 | 2600 |
| Three-dimensional simulations | | | | | | | | |
| 3D1 | 0.134 | 0.2 | 2, 2, 1 | 2000 | 0.054 | 0 | 0.746 | 2000 |
| 3D2 | 0.268 | 0.4 | 4, 4, 2 | 2000 | 0.054 | 0 | 0.746 | 2000 |
| 3D1-2600K | 0.134 | 0.2 | 2, 2, 1 | 2600 | 0.054 | 0 | 0.746 | 2600 |

where $\tau_f = H_{\text{jet},u}/u_{\text{jet}}$ is the timescale of the fluid based on the thickness and velocity of the jet, and $\tau_c$ is the chemical timescale, which is defined as the time it takes for a perfectly pre-mixed case to reach a CO-yield of 95% of the CO-yield in equilibrium. To make the DNS simulations computationally feasible, the computational domain (and the Reynolds number) has to be reduced in size compared to that of an industrial unit. The initial temperature of the simulation has therefore been increased to speed up conversion and make simulations feasible, and at the same time ensure that the Damköhler number remain small enough such that the effect of turbulence on the RWGS reaction can be studied. Somewhat arbitrarily, an initial temperature of 2000 K has therefore been chosen for the benchmark simulations. In order to initiate turbulence in the shear layers, some randomness is required. Here, randomness is introduced by adding low-amplitude initial Gaussian-distributed white noise in the velocity field. The amplitude of the noise is homogeneous over the volume and is set to slightly below 1% of the jet velocity.

#### 3.2.1. DNS

Given appropriate boundary conditions and accurate chemical kinetics, the DNS can be considered as numerical experiments because they resolve all temporal and spatial scales. It is therefore very useful to use DNS as validation cases for Large Eddy Simulations (LES). In this section we will present three different three-dimensional simulations that are characterized by different Damköhler and Reynolds numbers and that will later be used to validate the LES simulations. More specifications of these simulations are listed as Cases 3D1, 3D2 and 3D1-2600K in Tables 3 and 4.

In the following, the volumetric averaging of a variable $\phi$ is defined as

$$\langle \phi \rangle = \frac{1}{V_{\text{domain}}} \sum_{i,j,k} \phi(i,j,k) V, \tag{25}$$

the summation is over all three-dimensional indexes $i, j, k$, $V$ is the volume of a grid cell and $V_{\text{domain}}$ is the total volume of the domain.

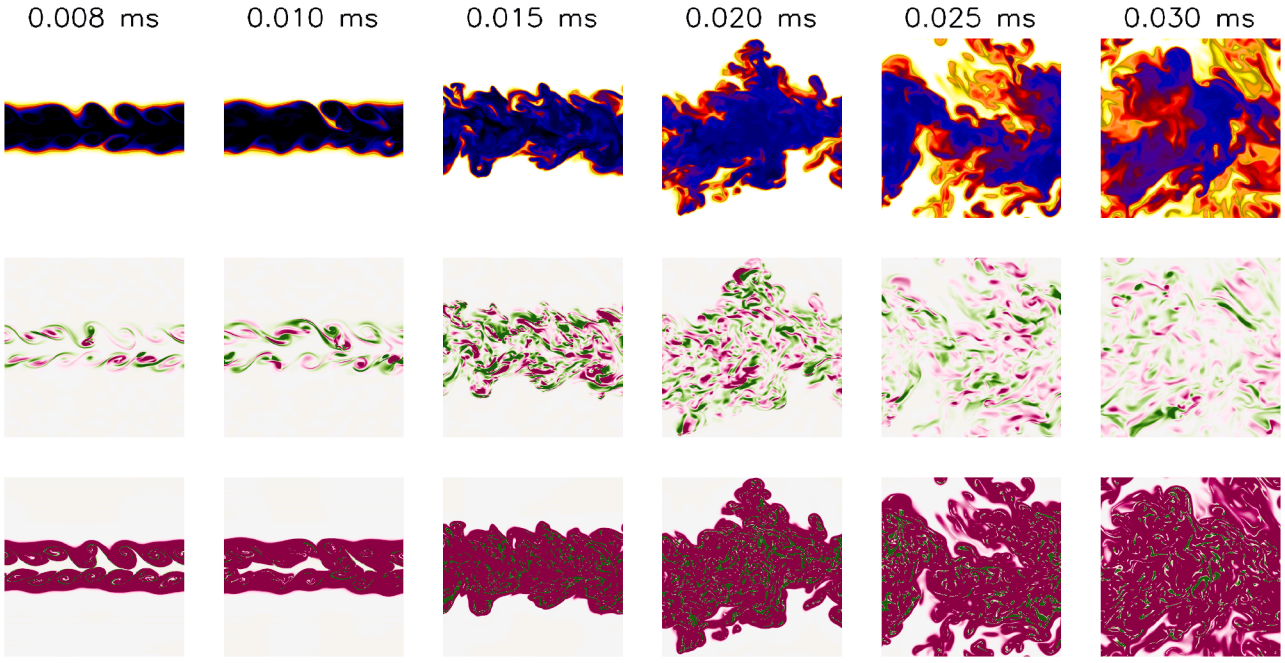


**Fig. 14.** Cross section of mixture fraction (upper row), vorticity in $x$-direction (middle row) and flame index (lower row) for case 3D1. For the flame index, negative values are represented by purple color while positive values have green color.

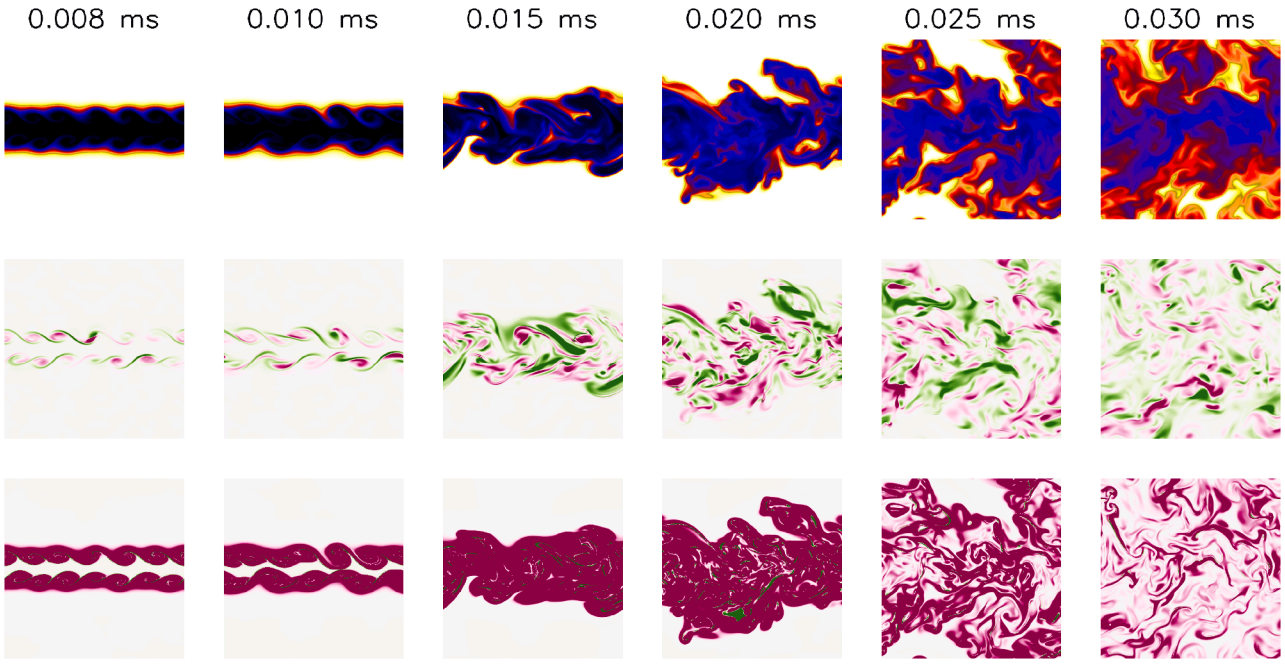


**Fig. 15.** Cross section of mixture fraction (upper row), vorticity in $x$-direction (middle row) and flame index (lower row) for case 3D1-2600K. For the flame index, negative values are represented by purple color while positive values have green color.

In Fig. 12, we compare characteristic time traces of integral quantities obtained from the DNS. The benchmark three-dimensional simulation (3D1) is presented by the thick black solid lines. Inspecting the two lower panels of the figure, we see that it takes about 0.01ms for the perturbations in the flow to grow the transversal velocities to their maximum. After this initial period of velocity growth, the turbulent decay results in a slow decay in turbulence intensity. Comparing results from the three-dimensional results with the corresponding two-dimensional results (black dashed lines), we see that the growth periods of the two simulations are pretty similar, but the decay is much slower for the two-dimensional simulation. This is due to the fact that in contrast to the direct turbulent cascade to *smaller* scales of a three-dimensional flow, a two-dimensional flow experience an indirect cascade to *larger* scales. Since turbulent dissipation occurs at small scales, the dissipation of energy is therefore much slower for a two-dimensional flow. Comparing the benchmark case with a three-dimensional simulation with higher Reynolds number (3D2 - blue solid lines in the figure), we see that for the higher Reynolds number case the turbulent decay is somewhat slower than for the benchmark case – as expected. The high-Reynolds number case is, however, too short to say anything very conclusive.

Moving now on to the mass fractions of $O_2$ and $H_2$, we see that they have a rather quick initial decrease, which becomes even steeper as soon

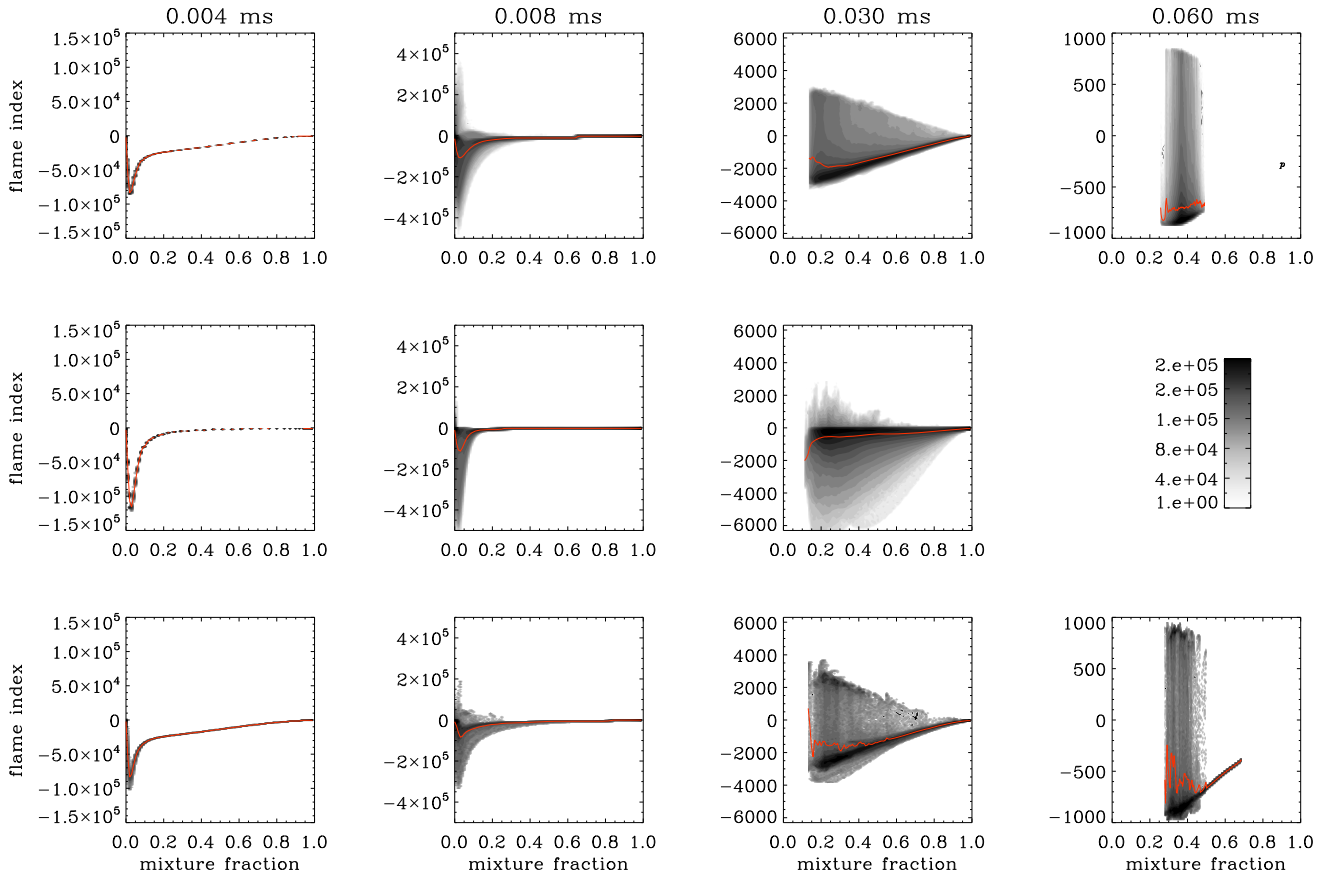


**Fig. 16.** Flame index (FI) for 3D1 (upper row) 3D1-2600K (middle row) and 2D1 (lower row). The red lines represent the average values.

**Table 4**
Initial parameters for the various simulations. For all cases, the mass fraction of helium is 0.2 in the jet and zero in the co-flow. Furthermore, the mass fraction of $CO_2$ is 0.746 in the jet and zero in the co-flow.

| | | timescales | | | Non-dim. params | | |
|---|---|---|---|---|---|---|---|
| Case | max($Y_{CO}$) – | $\tau_f$ [$10^{-7}$s] | $\tau_c$ [$10^{-7}$s] | $t_{CO}$ [$10^{-7}$s] | Da – | $t_{CO}/\tau_c$ – | *Re* – |
| Two-dimensional simulations | | | | | | | |
| 2D1 | 0.294 | 3.46 | 590 | 797 | 0.0059 | 1.35 | 1875 |
| 2D2 | 0.294 | 6.92 | 590 | 830 | 0.0117 | 1.40 | 3750 |
| 2D3 | 0.294 | 13.83 | 590 | 1100 | 0.0235 | 1.88 | 7500 |
| 2D1noO2 | 0.294 | 3.46 | 2880 | 3375 | 0.0012 | 1.17 | 1890 |
| 2D1x2O2 | 0.272 | 3.46 | 200 | 322 | 0.0173 | 1.61 | 1850 |
| 2D1-1800K | 0.292 | 3.46 | 5510 | 617 | 0.0006 | 1.12 | 2240 |
| 2D1-2200K | 0.295 | 3.46 | 105 | 279 | 0.033 | 2.66 | 1600 |
| 2D1-2400K | 0.295 | 3.46 | 36 | 210 | 0.096 | 5.84 | 1390 |
| 2D1-2600K | 0.295 | 3.46 | 18 | 206 | 0.198 | 11.79 | 1220 |
| Three-dimensional simulations | | | | | | | |
| 3D1 | 0.294 | 3.46 | 590 | NA | 0.0059 | NA | 1875 |
| 3D2 | 0.294 | 6.92 | 590 | NA | 0.0117 | NA | 3750 |
| 3D1-2600K | 0.295 | 3.46 | 18 | 195 | 0.198 | 11.15 | 1220 |

as turbulence has developed. The initial decrease is due to the partially pre-mixed initial boundary layer (with thickness $\delta_{shear}$) between the jet and the co-flow. As soon as the first turbulent eddies appear in the flow, the mixing due to them - and due to the following turbulence - quickly ensure that the $O_2$ in the jet mixes and reacts with $H_2$ in the co-flow, which results in a rather minor ($\sim$ 50 K) increase in average temperature of the mixture. This oxidation of $H_2$ with $O_2$ generates a large pool of OH, which in turn facilitates the conversion of $CO_2$ to CO, which is seen by the fact that the rate of CO production levels off at the time when the amount of OH in the mixture is reduced. This happens somewhat earlier for the benchmark case than for the case with higher Reynolds number (3D2). This effect of OH on the CO production is presented in more detail in Section 2.3. It is clear from these results that including some $O_2$ in the $CO_2$ stream has a positive effect on the CO production rate.

It is interesting to note that the results from the three-dimensional simulations are remarkably similar to those of the corresponding two-dimensional simulations (dashed lines). From the contour plots of mixture fraction and flame index for corresponding two- and three-dimensional simulations visualized in Fig. 13, we see that the similarity between the two simulations is relatively good at early times (0.02 ms) - before the turbulent cascade has become too important. At later times, however, the fundamental difference between the direct cascade of the three-dimensional flow and the inverse cascade of the two-dimensional flow becomes apparent by the scale difference of the dominating eddies. Later we will nevertheless utilize the early similarity between two and three dimensional simulations to perform affordable parameter studies using two-dimensional simulations.

Reducing the dimensionality of the simulation further to one dimension (dashed-dotted lines), no turbulence or vortex shedding is possible. Hence, mixing of species is due only to molecular mixing. It is clear from the one-dimensional results (dashed-dotted lines) that the lack of turbulence results in a much slower conversion of $CO_2$ - as expected.

Contour plots of vorticity, mixture fraction and flame index are visualized in Fig. 14 for case 3D1. From the last panels it can be seen that the extent of the domain in the y-direction is too small to contain all the turbulent flow. Since all boundary conditions are periodic, this means that in reality these simulations correspond to the infinite row of jets

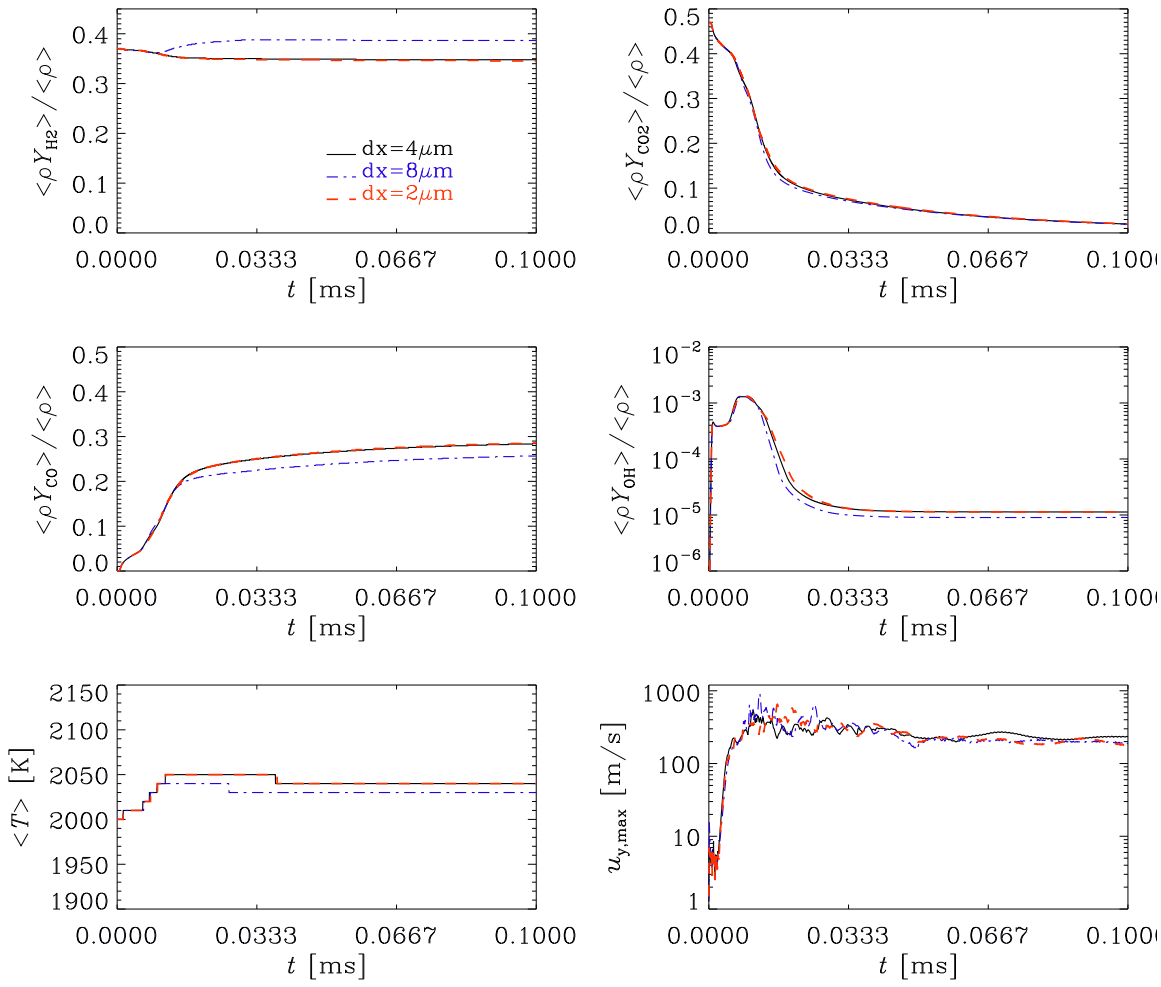


**Fig. 17.** Grid-independence study for case 2D1. The production resolution $\Delta x = 4\ \mu$m (black solid line) is compared with a coarsened grid $\Delta x = 8\ \mu$m (blue dash-dotted line) and a refined grid $\Delta x = 2\ \mu$m (red dashed line) on the same domain and with identical initial and boundary conditions.

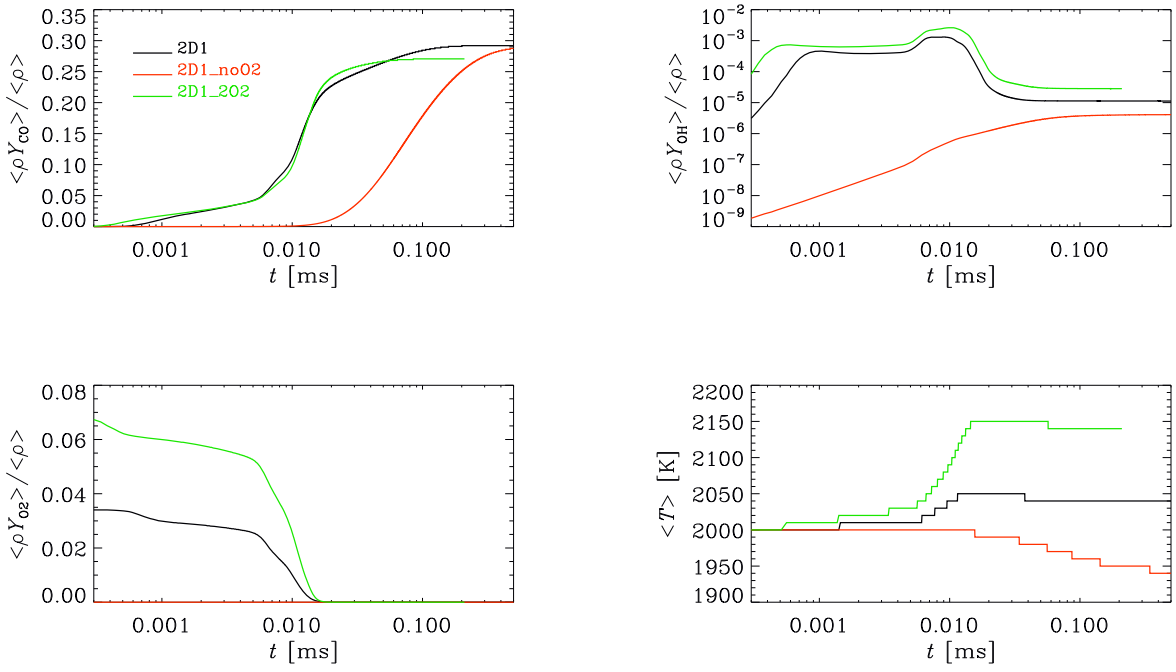


**Fig. 18.** Results for simulations with various amounts of $O_2$ in the initial jet stream.

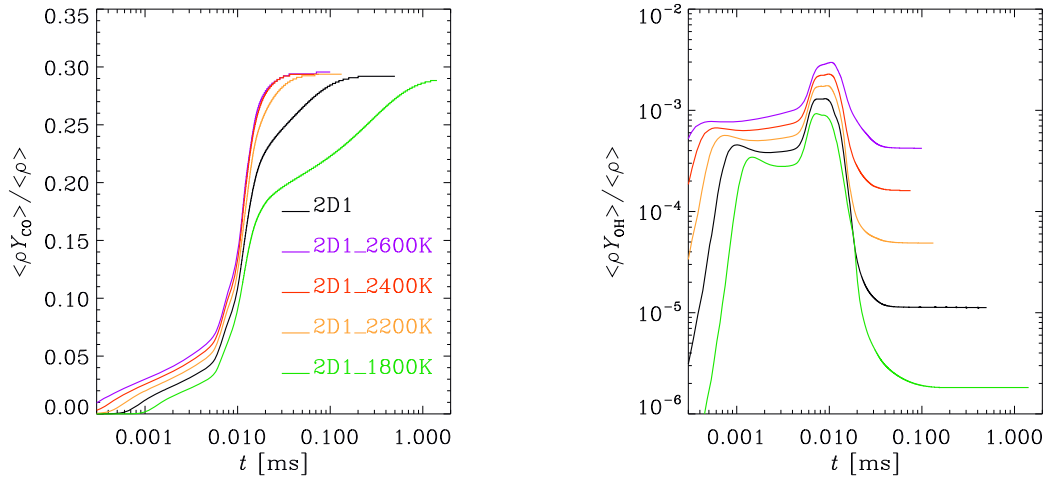


**Fig. 19.** Results for simulations with various initial temperatures.

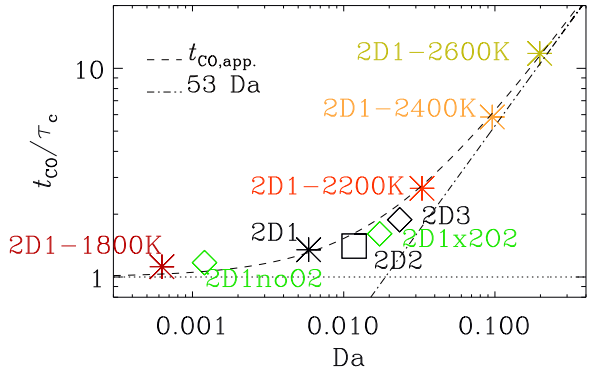


**Fig. 20.** Normalized time to reach 95% yield of CO as a function of Damköhler number.

in the y-direction, with the separation between each jet being equal to $L_y$. From the central panel, representing mixture fraction - with black corresponding to zero mixture fraction and white being a mixture fraction of unity - we see that after about 0.03 ms there is no pure $H_2$ left in the domain. Finally, for the flame index we see that although most of the reactions occur with negative flame index, there is also a significant amount of green zones, meaning positive flame index. As reactivity is decreased, the amount of green zones are expected to increase until the green volume equals the purple volume. For increasing reactivity, the opposite is expected. This can be seen by inspecting the lower row of Fig. 15, which shows the flame index for case 3D1-2600K, which has significantly higher reactivity than case 3D1. For 3D1-2600K we do indeed see much less green coloring in the flame index, as expected. It is also interesting to see that there is less fine structure in this high-temperature flow. This comes from the fact that the temperature is higher, yielding a higher viscosity.

The upper row of Fig. 16 shows a two-dimensional probability density function (PDF) of the flame index of simulation 3D1 as a function of mixture fraction for four different times. The legend of the PDF, corresponding to the number of cells with a given combination of FI and $z_H$, is show at the far right of the second row in the figure. At very early times, before any vortex generation in the boundary layer has occurred, we see from the left panel that the flame index is always negative. This is as expected since any reactions happening in the initial boundary layer between the two streams before mixing is initiated will proceed in non-premixed mode. As the time doubles to 0.008 ms, vortexes have already been generated from the shear and mixing has started. This is seen through the occurrence of the first positive contributions to the flame index. This only happens for very small mixture fractions, meaning that we are in very $CO_2$-rich environments. The reaction-weighted average is nevertheless always negative, as represented by the red line. At 0.03 ms, mixing has become stronger and we now see an almost symmetric profile around zero, indicating that a significant fraction of the total volume is reacting in premixed mode. The reaction weighted average is nevertheless negative. It can also be observed that the probability to find grid cells in the volume with mixture fraction below 0.15 is zero. This is because mixing has forced hydrogen-containing species into grid cell in the domain. At the very latest time (the far-right panel) the PDF of the flame index is still rather symmetric, although it continues to be somewhat skewed towards negative values. At this point, mixing has narrowed the available mixture-fraction space to the range between 0.25 and 0.5.

The middle row of Fig. 16 shows the PDF of the flame index as a function of mixture fraction for the case 3D1-2600K, which has a much larger Damköhler number than the previous case (3D1). This results in the flame index profile being consistently dominated by negative values. Only at the latest time is there a hint of positive values, but these are just very weak. This supports the assumption that a highly reactive case as 3D1-2600K experience almost only reactions in non-premixed mode.

Finally we compare the flame index PDF of three and two-dimensional cases, by comparing the results for 3D1 (upper row) with that of 2D1 (lower row). From the figure it can be seen that the PDFs are remarkably similar, at least for the three first times. The main difference for these three times is that the three-dimensional results are significantly smoother due to better statistics (more mesh points). Also the results for the latest time resemble each other, with the clear exception for a surprising line extending into larger mixture fractions for the two-dimensional results. The reason for this discrepancy becomes apparent by comparing the contour plots of the mixture fraction and flame index for the two simulations, as shown in Fig. 13. Here we see that the center of the large vortex of the two-dimensional simulation has higher mixture fraction than for the three-dimensional simulation. It can also be seen that the flame index inside this vortex is strongly correlated with the local mixture fraction. This results in the narrow peak in the PDF observed in the last panel of Fig. 16.

To verify that the production resolution is adequate, a grid-independence study was performed for case 2D1, in which the production resolution $\Delta x = 4\,\mu$m was both coarsened to $\Delta x = 8\,\mu$m and refined to $\Delta x = 2\,\mu$m, while keeping the domain, the initial conditions and the boundary conditions unchanged. The two-dimensional case is sufficient for this study since the sharpest gradients are encountered in the initial phase of the simulation, before any real three-dimensional

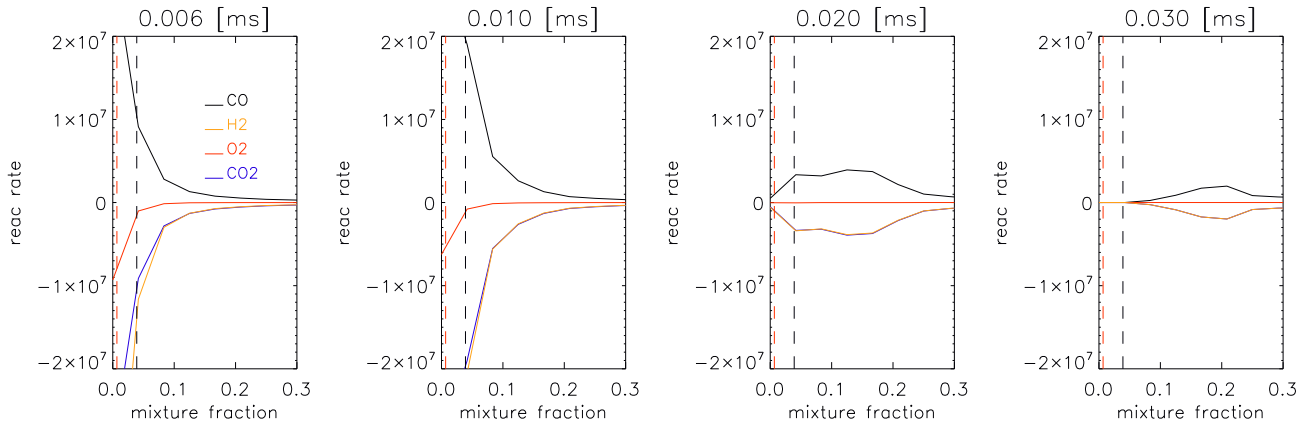


**Fig. 21.** Reaction rates as a function of $z_H$ for simulation 2D1 as defined in Table 3. The vertical dashed black and red lines represent stoichiometric mixture fractions based on $CO_2$ and $O_2$, respectively.

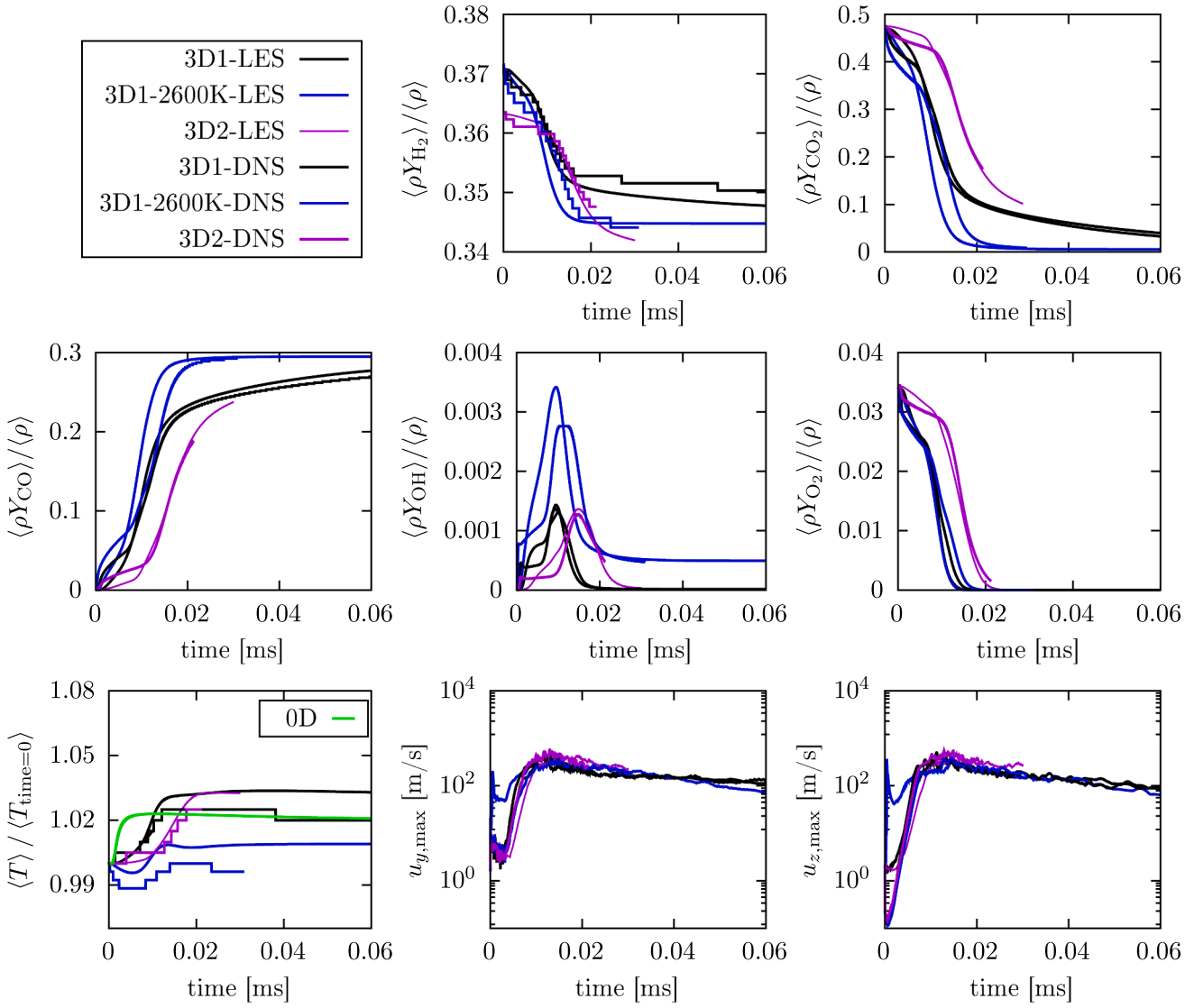


**Fig. 22.** Integral quantities for the LES (solid lines) cases 3D1 (black), 3D1-2600K (pink) and 3D2 (blue) compared with the corresponding DNS results (dashed lines).

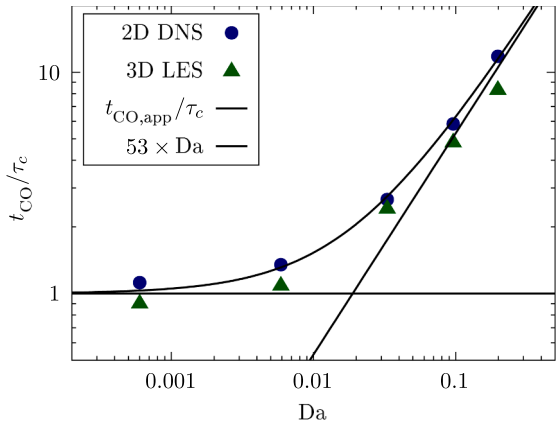


**Fig. 23.** Normalized time to reach 95% yield of CO as a function of Damköhler number, $t_{CO}/\tau_c$, as a function of the Damköhler number Da, where $t_{CO,app}$ is from Eq. (27).

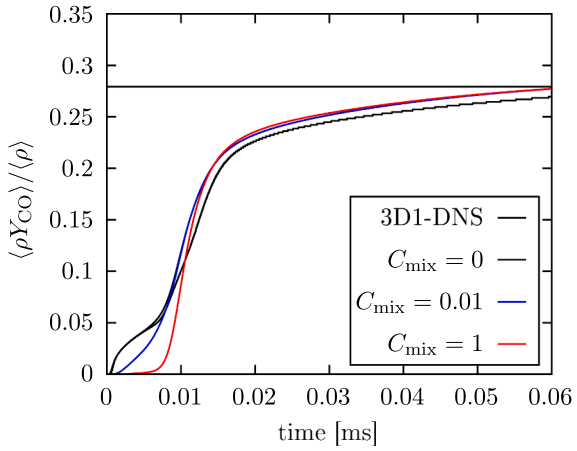


**Fig. 24.** Evolution of the CO-yield for the case 3D1 and different values of $C_{mix}$.

turbulence has developed, so that a resolution that yields a stable and grid-independent two-dimensional solution will also be sufficient for the corresponding three-dimensional simulation. The resulting time traces of the integral quantities are compared in Fig. 17. The production grid ($\Delta x = 4\,\mu$m) and the refined grid ($\Delta x = 2\,\mu$m) are essentially indistinguishable for all quantities, including the sensitive OH pool and the final CO yield, which demonstrates that the production resolution is sufficiently fine that the solution has reached grid independence. The Pencil Code is a high-order explicit DNS code with very little numerical diffusion, and an under-resolved mesh will therefore typically cause the simulation to blow up. This is indeed what happened for the coarsest grid ($\Delta x = 8\,\mu$m), which is why a high-frequency filtering had to be added in order to make that simulation run at all. The deviation of the coarsest grid seen in Fig. 17 – most notably the lower yield of CO and the reduced late-time OH level – is a direct consequence of this under-resolution and the associated filtering, and further confirms that resolutions at or below $\Delta x = 4\,\mu$m are required for a grid-independent solution.

### 3.2.2. *The impact of initial* $O_2$

It is interesting to see what happens when the $O_2$ in the jet is substituted with inert $N_2$, which is visualized in Fig. 18. (Please note that the x-axis is logarithmic for this and the next figure.) From the figure it becomes clear that without $O_2$ in the jet, it takes 4–5 times longer to reach full yield of CO without any $O_2$ in the initial jet. In particular it can be seen that without $O_2$ in the mixture, it takes long to build a sufficiently large pool of OH, and it is not until $t \sim 0.015$ s that the OH pool is large enough to facilitate any significant production of CO. Also, since the maximum level of OH is several orders of magnitude smaller without $O_2$ in the initial mixture, the maximum production rate of CO is also much lower (remember that the x-axis is logarithmic) than for the case with $O_2$. Given the significant benefit on conversion time of adding $O_2$ to the $CO_2$ stream, it is tempting to increase the amount of $O_2$ even further. However, from the green line in Fig. 18, it is clear that doubling the amount of $O_2$ does not result in any significant further speed-up compared to the original amount of $O_2$. This can be explained by the fact that, despite the amount of OH being somewhat higher for the case with double amount of $O_2$, the difference is not very large. Instead, we see that the final yield of CO is lower, since more of the $H_2$ is consumed by the additional $O_2$.

### 3.2.3. *Temperature dependence*

The reactivity of the mixture is very sensitive to the initial temperature. In Fig. 19, the temporal evolution for simulations with different initial temperatures are shown. It is clear that reducing the temperature to 1800 K, significantly increases the time to reach equilibrium (by around one order of magnitude). On the other hand, increasing the temperature to 2200 K, reduces the time to reach equilibrium, but a further increase in temperature to 2400 K, and eventually to 2600 K, has little effect on the production rate of CO. The reason that a further increase in temperature beyond 2200 K does not result in a corresponding reduction in conversion time, is that for these high reactivities it is the turbulent mixing that limits the conversion, not the kinetic reactivity. This is also reflected in the Damköhler number, which in Table 4 is shown to increase more than tenfold, from 0.0117 for the case with 2000 K, to 0.198 for 2600 K.

Varying the relationship between the chemical ($\tau_c$) and fluid ($\tau_f$) timescales results in different Damköhler numbers (see Eq. (24)). We know that for very large Damköhler numbers, which means that reactions are mixing controlled, the time to reach equilibrium should scale linearly with the fluid timescale, $\tau_f$. For the opposite extreme, when the Damköhler number is very small, the time to reach equilibrium should equal the chemical timescale, $\tau_c$. In the following, we approximate the time to reach equilibrium with the time it takes to reach a CO-yield of 95% of the equilibrium yield, as represented by $t_{CO}$. Based on the above, we end up with the following expressions for the value of $t_{CO}/\tau_c$ for the two extremes of the Damköhler number:

$$t_{CO}/\tau_c = \begin{cases} 1 & : \quad \mathrm{Da} \ll 1 \\ \alpha \mathrm{Da} & : \quad \mathrm{Da} \gg 1 \end{cases} \tag{26}$$

where $\alpha$ is a case dependent scaling factor. To test this expression we plot $t_{CO}/\tau_c$ as a function of Da in Fig. 20. In this figure, the horizontal dotted line corresponds to $t_{CO}/\tau_c = 1$, while the angled dashed-dotted line represent $t_{CO}/\tau_c = 53\mathrm{Da}$, i.e.; $\alpha$ is 53. From the figure we clearly see that for the smallest and the largest Damköhler numbers, the value of $t_{CO}/\tau_c$ approach the limiting lines as defined in Eq. (26). For the current geometry, we therefore propose the following analytical expression, which has a maximum of 20% error;

$$t_{CO,app.} = (1 + \alpha \mathrm{Da})\tau_c, \tag{27}$$

which is visualized by the dashed line in Fig. 20. The fitted scaling factor $\alpha = 53$ in Eq. (27) is specific to the temporal-jet geometry studied here, in which the entire mixing is driven by a single shear layer between two parallel streams. The same expression is expected to apply, with $\alpha$ of comparable magnitude, to other free shear flows of the same topology (e.g. planar or round jets in co-flow), since the entrainment rate per $\tau_f$ scales in the same way. For geometries with fundamentally different mixing dynamics, such as jet-in-cross-flow configurations, $\alpha$ must be refitted. The residual 20% error in the crossover region around $\mathrm{Da} \sim 1/\alpha$ reflects (i) the deliberate choice of using a simple linear blending of the two asymptotic limits without introducing any tunable parameters, and (ii) the fact that a single Damköhler number cannot resolve the distribution of local mixing-to-chemistry timescales that controls conversion at

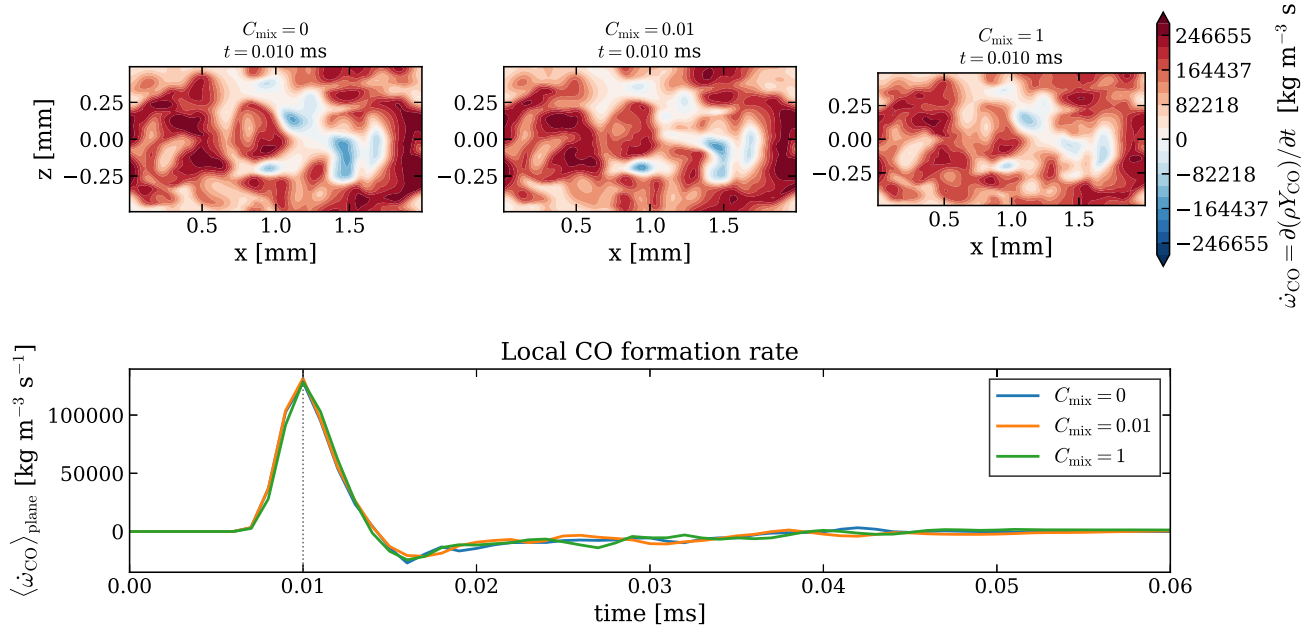


**Fig. 25.** Sensitivity of the local reaction rate to the PaSR mixing constant for case 3D1. Top row: local CO formation rate $\dot{\omega}_{\mathrm{CO}} = \partial(\rho Y_{\mathrm{CO}})/\partial t$ on the mid-plane at the most intense stage ($t \approx 0.01$ ms) for $C_{\mathrm{mix}} = 0$, 0.01, 1.0. Bottom: plane-averaged CO formation rate versus time for the same three values; the dotted line marks $t = 0.01$ ms.

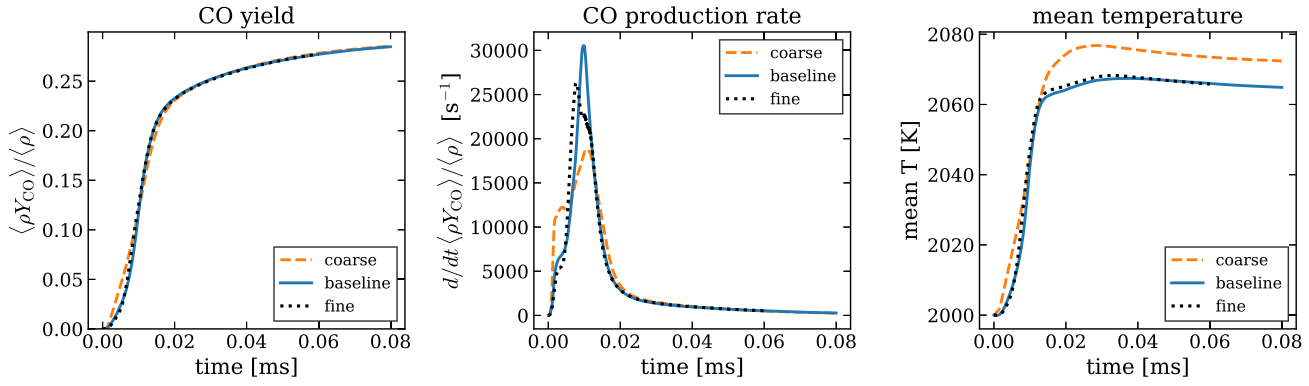


**Fig. 26.** LES grid convergence for case 3D1: density-weighted mean CO yield (left), CO production rate (centre) and volume-mean temperature (right) for the coarse ($64 \times 64 \times 32$), production ($128 \times 128 \times 64$) and fine ($256 \times 256 \times 128$) grids on the same $2 \times 2 \times 1$ mm domain.

intermediate Da, where the OH-mediated pathway of Section 2.3 couples both timescales non-trivially. The above expression does include all effects of variable Lewis numbers, which is critical when handling very light species such as hydrogen. Due to the weak endothermicity of the RWGS reaction, there are only small temperature gradients in these flows. The Soret effect is therefore not included.

#### 3.2.4. Reaction rates

It is known from non-premixed flames that the reaction rate typically peaks for mixture fractions around the stoichiometric mixture fraction. As we see from Fig. 21, this is not the case for the RWGS reaction. Instead, we see a much broader distribution in reaction rates as function of mixture fractions, and the peak of these distributions is not related to the stoichiometric mixture fraction. This is yet another example where we see clear differences between the endothermic RWGS and flames.

### 3.3. LES

In Fig. 22 we show the corresponding time traces computed by the LES as presented for the DNS in Fig. 12. Here, direct comparison of the three-dimensional cases between the LES (solid lines) and DNS (dashed lines) is offered. From the velocity time traces (lower panels) we observe excellent agreement on the shear-layer breakup time (about 0.01ms), a prerequisite for further comparison. It should be noted that the LES and DNS are initialized with similar noise levels ( $\sim 1\%$ of the jet-velocity) in all three directions, however, as seen from the maximum $z$-velocity component, the DNS notably features a strong decay of the artificial fluctuations, while the LES sustains the initial perturbations in the $z$ direction. Overall, the peak values and qualitative shape of the observed velocity traces agree reasonably well for the three cases considered. Comparing the mass fraction integrals we see good agreement in the overall

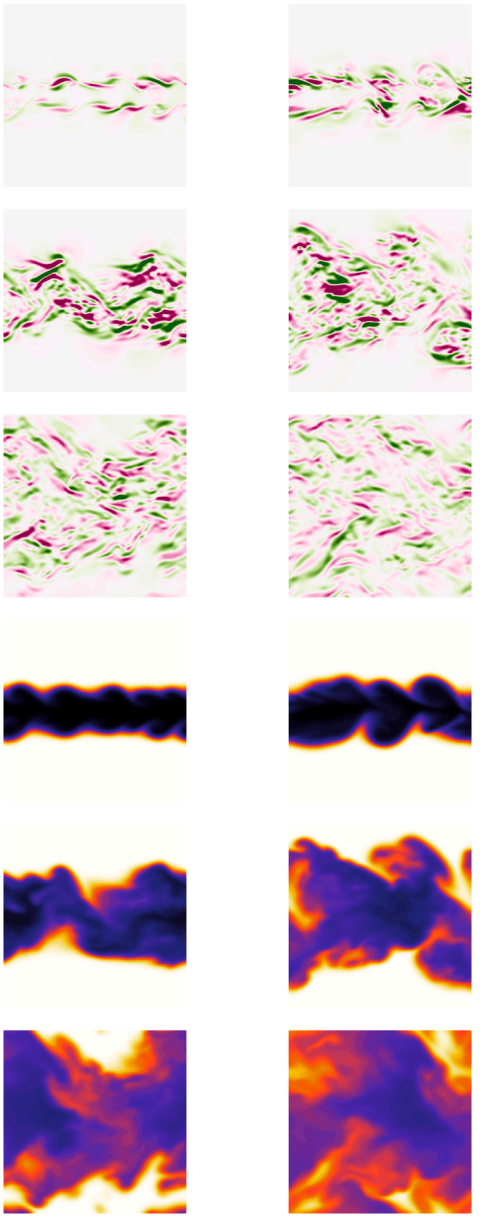

**Fig. 27.** Evolution of the jet for the case 3D1 at $t = 0.008$, 0.010, 0.015, 0.020, 0.025, and 0.030 ms illustrated by contour plots of the vorticity $x$-component (first row) and the mixture fraction (second row).

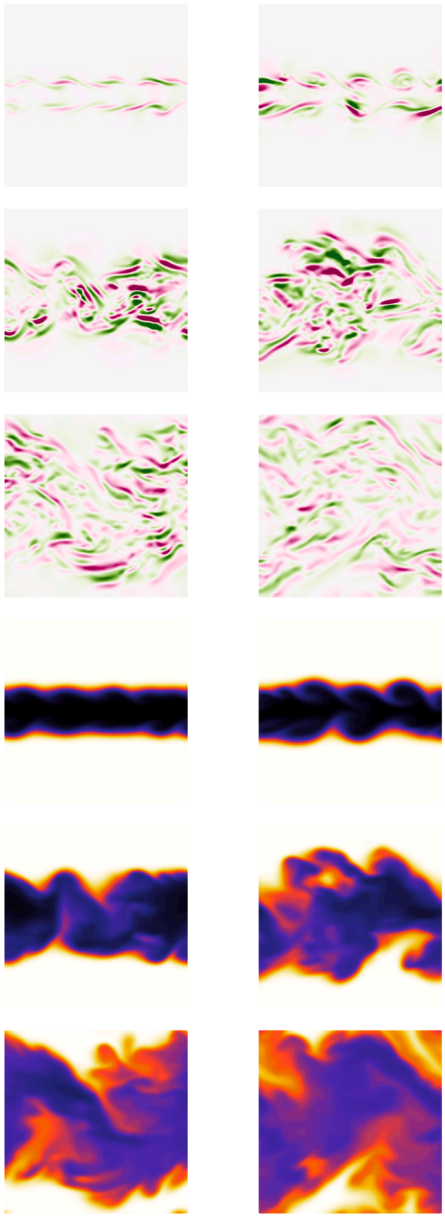

**Fig. 28.** Evolution of the jet for the case 3D1-2600K at $t = 0.008$, 0.010, 0.015, 0.020, 0.025, and 0.030 ms illustrated by contour plots of the vorticity $x$-component (first row) and the mixture fraction (second row).

time evolution, specifically at later times, with the equilibrium correctly quantified in the LES. Further, the time to conversion, indicated by the CO integrals crossing the dotted 95% CO-yield line, is predicted to within 10% of the DNS results. During the initial phase (up to 0.01ms), the effect of choosing a finite $C_{\text{mix}}$ in the LES model becomes apparent: In the DNS the entire computational cell is allowed to react, while in the LES the reaction rates are modulated, producing a slightly slower CO and OH production. The average temperature profiles predicted by the LES agree well with the DNS, since for all three cases, the difference relative to the initial value is $\sim 1\%$.

Fig. 23 illustrates the normalized time required to reach 95% CO yield, $t_{\text{CO}}/\tau_c$, as a function of the Damköhler number (Da), where $t_{\text{CO,app}}$ is from Eq. (27). The DNS and LES results show qualitative agreement, following the same trend with respect to Da. However, the LES results consistently lie slightly below the DNS results for all examined Da values. This discrepancy may be attributed to the higher average temperatures predicted by LES compared to DNS, as seen in Fig. 22, since elevated temperatures accelerate chemical reactions and thus conversion. The same figure also includes results from a zero-dimensional (0D) simulation using the same chemical kinetics scheme, also performed in OpenFOAM, but without PaSR (green solid line in Fig. 22). The initial condition of this 0D simulation is identical to the mass-averaged initial condition of the cases 3D1-DNS and 3D1-LES, and we see from Fig. 22 that the final temperature of the 0D case equals that of the 3D1-DNS case. Furthermore, the 0D simulation also yields a conversion time $t_{\text{CO}}$ that is the same as obtained for 0D simulations with the Pencil-Code, supporting the interpretation that elevated temperatures in the three-dimensional LES are the reason for the lower $t_{\text{CO}}$ found for 3D-LES simulations.

Fig. 24 shows the CO production integral for three different values of $C_{\text{mix}}$, compared to the DNS results. The values $C_{\text{mix}} \in \{0, 1\}$ correspond to $\tau_{\text{mix}} \in \{0, \sqrt{\nu_{\text{eff}}/\epsilon}\}$. Notably, when switching off the PaSR model ($C_{\text{mix}} = 0$), and $\kappa = 1$, which considers the entire cell volume to be reactive, as in the DNS. The intermediate value ($C_{\text{mix}} = 0.01$), represents

the situation where cell resolution constraints are in place. We see that there are significant deviations during the initial phase, before the shear layer breaks up and turbulent mixing is negligible. After ~ 0.012ms, the integrals for different $C_{\mathrm{mix}}$ are indistinguishable, giving confidence that the chosen value of $C_{\mathrm{mix}} = 0.01$ can be considered reasonable to fix for all simulations. It should be noted that taking $C_{\mathrm{mix}} = 0$ gives the best agreement with the DNS for this specific study, however, as the goal is to test a *viable* LES model for later use on an industrial scale reactor, the resolutions will vary, hence a value of $C_{\mathrm{mix}} = 0$ is unrealistic for future work; as $C_{\mathrm{mix}} = 0.01$ gives good agreement, we choose this value.

While the integrated CO yield in Fig. 24 establishes that the final conversion is insensitive to $C_{\mathrm{mix}}$, another concern is the *local* reaction rate at the most intense stage. We therefore compare the local CO formation rate $\dot{\omega}_{\mathrm{CO}} = \partial(\rho Y_{\mathrm{CO}})/\partial t$ on the mid-plane at $t \approx 0.01$ ms (the instant of peak plane-averaged rate) in Fig. 25, for the same three runs with $C_{\mathrm{mix}} \in \{0,\ 0.01,\ 1.0\}$. The three simulations are otherwise identical in mesh, inlet composition, temperature and mechanism. Both the local rate fields (top row) and the plane-averaged rate (bottom panel) change only marginally across the two orders of magnitude in $C_{\mathrm{mix}}$, so the low sensitivity of the integrated conversion also holds for the local rates.

In Fig. 26, we compare the reference resolution, $128 \times 128 \times 64$, with a coarsened $64 \times 64 \times 32$ and a refined $256 \times 256 \times 128$ grid for case 3D1, on the same $2 \times 2 \times 1$ mm domain, with $C_{\mathrm{mix}} = 0.01$ and all initial and boundary conditions held fixed. The density-weighted mean CO yield $\langle \rho Y_{\mathrm{CO}} \rangle / \langle \rho \rangle$ and the volume-mean temperature, change only marginally between the production and finest grids, indicating that the production grid is adequately resolved, consistent with its near-DNS resolution across the reaction zone. The instantaneous peak reaction rate is more sensitive to resolution, but its sensitivity lessens with successive refinement, consistent with the solution approaching grid independence.

Contour plots of the vorticity $x$-component and the mixture fraction as computed by the LES are illustrated in Fig. 27. There is overall qualitative agreement in the time evolution of the flow field in terms of jet-breakup dynamics and $H_2$ conversion, cf. Fig. 14, showing the mixture fraction with black color denoting zero mixture fraction (no elemental hydrogen) and white representing a mixture fraction of unity (co-flow composition). Similarly to the evolution of the DNS jet, we see that after approximately 0.03 ms there is almost no pure $H_2$ left in the domain. From the mixture fraction snapshots we also observe the same trend in terms of slightly slower dynamics for the 2600 K vs 2000 K simulations, as in the DNS. We also clearly observe the filtering effect of the LES, yielding less fine structures than the DNS. Similarly to the DNS results, the higher viscosity in the 3D1-2600K case, shown in Fig. 28, also produces larger flow structures.

## 4. Conclusions

Comparing the reaction rates of various syngas mechanisms under conditions relevant to the RWGS reaction shows that all the detailed syngas mechanisms studied here yield comparable results. Global reaction mechanisms should not be used though, since they do not account for the forward water-gas-shift reaction, and hence, they are not able to predict the equilibrium. For this study the two smallest mechanisms are therefore used, since they are more computationally efficient than the larger ones. At atmospheric pressure, it is found that just very minor traces of $O_2$ can have a strong effect on the rate of the RWGS reaction. Since existing experimental tests of the non-catalytic reverse water-gas-shift reaction do not provide data on the level of $O_2$ at the inlet at sufficiently high accuracy, it is not possible to validate the performance of the syngas reaction mechanisms against the currently available experimental data. At high pressures and temperatures, relevant for non-catalytic RWGS, the free-radical promoted effect of $O_2$ is, however, less pronounced than at atmospheric pressure.

The temporal jet framework is used to investigate the turbulence-chemistry interactions of the RWGS reaction. Form the flame index it is found that for an initial temperature of 2600 K, essentially all reactions proceed in non-premixed mode, while already at a temperature of 2000 K, a significant fraction of the $CO_2$ conversion proceeds in a premixed mode.

At 30 bars, having 5% $O_2$ in the $CO_2$-stream results in a 2–3 times shorter conversion time than without $O_2$. Doubling the amount of $O_2$ beyond this has, however, little effect on the conversion rate except that less CO is produced due to the extra oxidation.

For the temporal jet configuration studied in this paper, an algebraic description of the time to reach 95% conversion of CO is proposed; see Eq. (27). The resulting expression for $t_{\mathrm{CO}}$, which is a function of the Damköhler number and the chemical timescale, accounts for the effects of Reynolds number, oxygen level, and temperature (as can be seen from Fig. 20). As such, this equation can be used to *a priori* give an estimate of the conversion time for turbulent shear flows.

Finally, we compared the DNS results with those of the corresponding LES, which use a dynamic one-equation subgrid-scale eddy viscosity model, together with the PaSR model for turbulence chemistry interactions. Despite the fact that the PaSR model is developed with strongly exothermic flames in mind, the comparison shows that the current LES-setup is able to nicely reproduce the DNS results even for the endothermic RWGS reaction.

The present paper shows that, by comparing with DNS, the LES with the PaSR model can be used for endothermic reactions at small scales. Recommended additional work is then to validate the combination of turbulence modeling and chemical kinetics used in LES against experimental results at larger scale. For proper validation it is critical that all boundary conditions of the experiments are well known and that sufficient measurements data are obtained.

## CRediT authorship contribution statement

**Nils Erland L. Haugen:** Writing – review & editing, Writing – original draft, Visualization, Supervision, Software, Resources, Project administration, Methodology, Investigation, Funding acquisition, Formal analysis, Data curation, Conceptualization; **Axel Brandenburg:** Writing – review & editing, Writing – original draft, Visualization, Supervision, Software, Resources, Methodology, Investigation, Formal analysis, Data curation, Conceptualization; **Ewa Karchniwy:** Writing – original draft, Visualization, Investigation, Data curation; **Ole Hauke Heinz Meyer:** Writing – original draft, Visualization, Validation, Investigation, Data curation; **Åsmund Ervik:** Supervision, Project administration, Methodology, Investigation, Funding acquisition, Data curation, Conceptualization; **Hursanay Fyhn:** Visualization, Investigation, Data curation; **Ladan Samaei:** Data curation, Conceptualization; **Bjørn Bringedal:** Writing – original draft, Supervision, Resources, Project administration, Methodology, Funding acquisition, Conceptualization.

## Declaration of generative AI and AI-assisted technologies in the manuscript preparation process

During the preparation of this work, the author(s) used Claude for text review. The author(s) reviewed and edited the output as needed and take full responsibility for the content of the published article.

## Declaration of competing interest

The authors declare the following financial interests/personal relationships which may be considered as potential competing interests: Nils Erland L. Haugen reports financial support was provided by Research Council of Norway. Bjoern Bringedal reports financial support was provided by Nordic electrofuel AS. Hursanay Fyhn reports financial support was provided by Research Council of Norway. Ewa Karchniwy reports financial support was provided by Research Council of Norway. Ole Meyer reports financial support was provided by Research Council of Norway. Aasmund Ervik reports financial support was provided by Research Council of Norway. Ladan Samaei reports financial support

was provided by Nordic Electrofuel AS. Bjoern Bringedal reports a relationship with Nordic Elerctrofuel AS that includes: employment. Ladan Samaei reports a relationship with Nordic Electrofuel that includes: employment. Bjoern Bringedal has patent pending to assignee. If there are other authors, they declare that they have no known competing financial interests or personal relationships that could have appeared to influence the work reported in this paper.

## Acknowledgments

Funding from the Norwegian research council through the SAFIRE project (346574) is acknowledged. We also acknowledge the allocation of computing resources provided through the Norwegian Sigma2 project through allocation No. NS11020K.

## Data availability

Data will be made available on request.

## References

Babkovskaia, N., Haugen, N.E.L., Brandenburg, A., 2011. A high-order public domain code for direct numerical simulations of turbulent combustion. J. Comput. Phys. 230 (1), 1–12. https://doi.org/10.1016/j.jcp.2010.08.028

Benzinger, W., Daymo, E., Hettel, M., Maier, L., Antinori, C., Pfeifer, P., Deutschmann, O., 2019. Reverse water gas shift (RWGS) over ni - spatially-resolved measurements and simulations. Chem. Eng. J. 362, 430–441. https://doi.org/10.1016/j.cej.2019.01.038

Bradford, B.W., 1933. The water-gas reaction in low-pressure explosions. J. Chem. Soc. 1557–1563. https://doi.org/10.1039/JR9330001557

Bustamante, F., Enick, R.M., Cugini, A.V., Killmeyer, R.P., Howard, B.H., Rothenberger, K.S., Ciocco, M.V., Morreale, B.D., Chattopadhyay, S., Shi, S., 2004. High-temperature kinetics of the homogeneous reverse water-gas shift reaction. AIChE J. 50 (5), 1028–1041. https://doi.org/10.1002/aic.10099

Cook, A., 2009. Enthalpy diffusion in multicomponent flows. Phys. Fluids 21, 055109. https://doi.org/10.1063/1.3139305

Davis, S.G., Joshi, A.V., Wang, H., Egolfopoulos, F., 2005. An optimized kinetic model of h2/CO combustion. Proc. Combust. Inst. 30 (1), 1283–1292. https://doi.org/10.1016/j.proci.2004.08.252

Desgagnés, A., Iliuta, I., Iliuta, M.C., 2024. Sorption-enhanced intensified CO2 hydrogenation via reverse water-gas shift reaction: kinetics and modelling. Chem. Eng. J. 494, 152052. https://doi.org/10.1016/j.cej.2024.152052

Ebrahimi, P., Kumar, A., Khraisheh, M., 2022. A review of ceo2 supported catalysts for CO2 reduction to CO through the reverse water gas shift reaction. Catalysts 12 (10). https://doi.org/10.3390/catal12101101

Fayisa, B.A., Yang, Y., Zhen, Z., Wang, M.Y., Lv, J., Wang, Y., Ma, X., 2022. Engineered chemical utilization of CO2 to methanol via direct and indirect hydrogenation pathways: a review. Ind. Eng. Chem. Res. 61 (29), 10319–10335. https://doi.org/10.1021/acs.iecr.2c00402

Frassoldati, A., Faravelli, T., Ranzi, E., 2007. The ignition, combustion and flame structure of carbon monoxide/hydrogen mixtures. note 1: detailed kinetic modeling of syngas combustion also in presence of nitrogen compounds. Int. J. Hydrog. Energy 32 (15), 3471–3485. International Symposium on Solar-Hydrogen-Fuel Cells 2005. https://doi.org/10.1016/j.ijhydene.2007.01.011

Fureby, C., 2012. A comparative study of flamelet and finite rate chemistry LES for a swirl stabilized flame. J. Eng. Gas Turbines Power 134 (4), 041503–041503–13. https://doi.org/10.1115/1.4004718

Ghodoosi, F., Khosravi-Nikou, M.R., Shariati, A., 2017. Mathematical modeling of reverse water-gas shift reaction in a fixed-bed reactor. Chem. Eng. Technol. 40 (3), 598–607. https://doi.org/10.1002/ceat.201600220

Goodwin, D.G., Moffat, H.K., Schoegl, I., Speth, R.L., Weber, B.W., 2023. Cantera: An object-oriented software toolkit for chemical kinetics, thermodynamics, and transport processes. Version 3.0.0. https://doi.org/10.5281/zenodo.8137090

Graven, W.M., Long, F.J., 1954. Kinetics and mechanisms of the two opposing reactions of the equilibrium CO + h2o = CO2 + h2. J. Am. Chem. Soc. 76 (10), 2602–2607. https://doi.org/10.1021/ja01639a002

Gruber, A., Meyer, O. H.H., Heggset, T., Wood, B., Ciani, A., 2024. Numerical investigation of reheat hydrogen flames in the sequential-combustion stage of a heavy-duty gas turbine. Vol. Volume 3B: Combustion, Fuels, and Emissions of *Turbo Expo: Power for Land, Sea, and Air*, p. V03BT04A055. https://doi.org/10.1115/GT2022-83218

Hawkes, E.R., Sankaran, R., Sutherland, J.C., Chen, J.H., 2007. Scalar mixing in direct numerical simulations of temporally evolving plane jet flames with skeletal CO/h2 kinetics. Proc. Combust. Inst. 31 (1), 1633–1640. https://doi.org/10.1016/j.proci.2006.08.079

Heggset, T., Meyer, O. H.H., Gruber, A., Tay-Wo-Chong, L., Ciani, A., 2024a. Combustion optimization and burnout of ammonia-based gaseous fuels in the constant pressure sequential combustion system operated in rich-quench-lean mode. Vol. Volume 3B: Combustion, Fuels, and Emissions of *Turbo Expo: Power for Land, Sea, and Air*, p. V03BT04A054. https://doi.org/10.1115/GT2024-128946

Heggset, T., Meyer, O. H.H., Tay Wo Chong Hilares, L., Ciani, A., Gruber, A., 2024b. Numerical assessment of a rich-quench-lean staging strategy for clean and efficient combustion of partially decomposed ammonia in the constant pressure sequential combustion system. J. Eng. Gas Turbines Power 146(8), 081004. https://doi.org/10.1115/1.4063958

Hernandez Lalinde, J.A., Roongruangsree, P., Ilsemann, J., Bäumer, M., Kopyscinski, J., 2020. Co2 methanation and reverse water gas shift reaction. kinetic study based on in situ spatially-resolved measurements. Chem. Eng. J. 390, 124629. https://doi.org/10.1016/j.cej.2020.124629

Kaskan, W.E., Browne, W.G., 1964. Kinetics of the $H_2/CO/O_2$ System. Rep. R64SD37. General Electric Space Sciences Laboratory.

Kim, W., Menon, S., 1995. A new dynamic one-equation subgrid-scale model for large eddy simulations. In: 33rd Aerospace Sciences Meeting and Exhibit. AIAA. https://doi.org/10.2514/6.1995-356

Kéromnès, A., Metcalfe, W.K., Heufer, K.A., Donohoe, N., Das, A.K., Sung, C.-J., Herzler, J., Naumann, C., Griebel, P., Mathieu, O., Krejci, M.C., Petersen, E.L., Pitz, W.J., Curran, H.J., 2013. An experimental and detailed chemical kinetic modeling study of hydrogen and syngas mixture oxidation at elevated pressures. Combust. Flame 160 (6), 995–1011. https://doi.org/10.1016/j.combustflame.2013.01.001

Li, W., Zou, C., Yao, H., Lin, Q., Fu, R., Luo, J., 2022. An optimized kinetic model for h2/CO combustion in CO2 diluent at elevated pressures. Combust. Flame 241, 112093. https://doi.org/10.1016/j.combustflame.2022.112093

Li, X., You, X., Wu, F., Law, C.K., 2015. Uncertainty analysis of the kinetic model prediction for high-pressure h2/CO combustion. Proc. Combust. Inst. 35 (1), 617–624. https://doi.org/10.1016/j.proci.2014.07.047

Meyer, O. H.H., Tay-Wo-Chong, L., Ciani, A., Gruber, A., 2026. Numerical concept study for part-load operation of the ansaldo constant pressure sequential combustion system operated in rich-dilute-lean mode using ammonia-based gaseous fuels. J. Eng. Gas Turbines Power 148 (5), 051015. https://doi.org/10.1115/1.4069843

Pencil Code Collaboration, Brandenburg, A., Johansen, A., Bourdin, P., Dobler, W., Lyra, W., Rheinhardt, M., Bingert, S., Haugen, N., Mee, A., Gent, F., Babkovskaia, N., Yang, C.-C., Heinemann, T., Dintrans, B., Mitra, D., Candelaresi, S., Warnecke, J., Käpylä, P., Schreiber, A., Chatterjee, P., Käpylä, M., Li, X.-Y., Krüger, J., Aarnes, J., Sarson, G., Oishi, J., Schober, J., Plasson, R., Sandin, C., Karchniwy, E., Rodrigues, L., Hubbard, A., Guerrero, G., Snodin, A., Losada, I., Pekkilä, J., Qian, C., 2021. The pencil code, a modular MPI code for partial differential equations and particles: multipurpose and multiuser-maintained. J. Open Source Softw. 6 (58), 2807. arxiv:2009.08231, https://doi.org/10.21105/joss.02807

Pomiro, F.J., Fouga, G.G., Bohé, A.E., Gayone, J.E., De Micco, G., 2024. Kinetic study of reverse water-gas shift chemical looping on la-based perovskite. J. Environ. Chem. Eng. 12 (2), 112317. https://doi.org/10.1016/j.jece.2024.112317

Qi, Y., Zhu, Y.-A., Chen, D., 2020. Mechanism investigation and catalyst screening of high-temperature reverse water gas shift reaction. Green Chem. Eng. 1 (2), 131–139. https://doi.org/10.1016/j.gce.2020.10.001

Rintanen, A., Morev, I., 2025. Personal Communication. Aalto University, Espoo, Finland.

Santos, M.F., Bresciani, A.E., Ferreira, N.L., Bassani, G.S., Alves, R. M.B., 2023. Carbon dioxide conversion via reverse water-gas shift reaction: reactor design. J. Environ. Manag. 345, 118822. https://doi.org/10.1016/j.jenvman.2023.118822

Shekari, A., Labrecque, R., Larocque, G., Vienneau, M., Simoneau, M., Schulz, R., 2023. Conversion of CO2 by reverse water gas shift (RWGS) reaction using a hydrogen oxyflame. Fuel 344, 127947. https://doi.org/10.1016/j.fuel.2023.127947

Starik, A.M., Titova, N.S., Sharipov, A.S., Kozlov, V.E., 2010. Syngas oxidation mechanism. Combust. Explos. Shock Waves 46, 491–506. https://doi.org/10.1007/s10573-010-0065-x

Sun, F., Yan, C., Wang, Z., Guo, C., Huang, S., 2015. Ni/ce-zr-o catalyst for high CO2 conversion during reverse water gas shift reaction (RWGS). Int. J. Hydrog. Energy 40 (46), 15985–15993. https://doi.org/10.1016/j.ijhydene.2015.10.004

Sun, H., Yang, S.I., Jomaas, G., Law, C.K., 2007. High-pressure laminar flame speeds and kinetic modeling of carbon monoxide/hydrogen combustion. Proc. Combust. Inst. 31 (1), 439–446. https://doi.org/10.1016/j.proci.2006.07.193

Tang, R., Zhu, Z., Li, C., Xiao, M., Wu, Z., Zhang, D., Zhang, C., Xiao, Y., Chu, M., Genest, A., Rupprechter, G., Zhang, L., Zhang, X., He, L., 2021. Ru-catalyzed reverse water gas shift reaction with near-unity selectivity and superior stability. ACS Mater. Lett. 3 (12), 1652–1659. https://doi.org/10.1021/acsmaterialslett.1c00523

Tingey, G.L., 1966. Kinetics of the water-gas equilibrium reaction. i. the reaction of carbon dioxide with hydrogen. J. Phys. Chem. 70, 1406-1412. https://doi.org/10.1021/j100877a011

Turányi, T., Tomlin, A.S., 2014. Analysis of Kinetic Reaction Mechanisms. Springer, Berlin, Heidelberg. https://doi.org/10.1007/978-3-662-44562-4

Weller, H.G., Tabor, G., Jasak, H., Fureby, C., 1998. A tensorial approach to computational continuum mechanics using object-oriented techniques. Comput. Phys. 12, 620–631. https://doi.org/10.1063/1.168744

Wolf, A., Jess, A., Kern, C., 2016. Syngas production via reverse water-gas shift reaction over a ni-al2o3 catalyst: catalyst stability, reaction kinetics, and modeling. Chem. Eng. Technol. 39 (6), 1040–1048. https://doi.org/10.1002/ceat.201500548

Yamaoka, M., Tomozawa, K., Sumiyoshi, K., Ueda, T., Ogo, S., 2024. Efficient reverse water gas shift reaction at low temperatures over an iron supported catalyst under an electric field. Sci. Rep. 14, 10216. https://doi.org/10.1038/s41598-024-61017-2

Zhang, Q., Bown, M., Pastor-Pérez, L., Duyar, M.S., Reina, T.R., 2022. Co2 conversion via reverse water gas shift reaction using fully selective mo-p multicomponent catalysts. Ind. Eng. Chem. Res. 61 (34), 12857–12865. https://doi.org/10.1021/acs.iecr.2c00305